Quantification of capillary rise dynamics in snow using neutron radiography

Michael Lombardo[1], Amelie Fees[1], Anders Kaestner[2], Alec van Herwijnen[1], Jürg Schweizer[1], and Peter Lehmann[3]

[1]WSL Institute for Snow and Avalanche Research SLF, Davos, Switzerland
[2]Laboratory for Neutron Scattering and Imaging, Paul Scherrer Institute, Villigen, Switzerland
[3]Physics of Soils and Terrestrial Ecosystems, ETH Zurich, Zurich, Switzerland

Correspondence: Michael Lombardo (michael.lombardo@slf.ch)

Abstract. Liquid water flow in snow is important for snow hydrology, remote sensing, and avalanche formation. Water flow in snow is often dominated by capillary effects, which are responsible for the formation of capillary barriers, capillary flow paths, and capillary rise. Unfortunately, there is little quantitative data on the capillary forces of snow, particularly with respect to capillary rise dynamics. Here, we present the results of 4 capillary rise experiments using neutron radiography. The experiments

5   were performed in $13 \times 13 \times 1 \, \mathrm{cm}^3$ glass columns with sand-snow and sand-gravel-snow layering mimicking the capillary forces at the soil-snow interface. Images were taken at 10 s to 15 s intervals with a pixel size of 92 μm. The experiments provided quantitative results of high resolution liquid water profiles, wetting front progression, flow rates, and parameterization of snow hydraulic properties. The experiments showed that the snow properties influenced the capillary rise height while the hydraulic properties of the transitional layer below the snow influenced the flow rates. The saturated hydraulic conductivity values

10   obtained from the experiments were below the expected values from the literature.

1 Introduction

The dynamics of liquid water flow in snow are important for snow hydrology (e.g., Quéno et al., 2020; Webb et al., 2020), remote sensing (e.g., Marin et al., 2020; Rösel et al., 2021), and avalanche forecasting (e.g., Wever et al., 2017; Hendrick et al., 2023). For example, snowmelt and rain-on-snow events are important for stream-flow predictions (e.g., Würzer et al.,

15   2017; Hammond and Kampf, 2020), while the first wetting of weak layers within the snowpack can lead to an increase in avalanche activity (Wever et al., 2018). In these examples, water is generated at the snow surface through melting or rain-on-snow events and subsequently percolates towards the ground. This percolation is known to be affected by capillary forces within the snowpack, through the formation of preferential flow paths (Hirashima et al., 2019) and capillary barriers (Quéno et al., 2020). In addition to top-down percolation, capillary rise has been shown to be relevant for the wicking of brine into

20   snow on sea ice (Mallett et al., 2024) and the formation of wet basal layers under gliding snowpacks (Mitterer and Schweizer, 2012; Lombardo et al., 2025b).

      The inclusion of capillary forces in snowpack models has been shown to improve the simulation results of water flow in snow (Wever et al., 2014; D'Amboise et al., 2017). For example, 2D simulations were able to generate preferential (Leroux

et al., 2020) and lateral flow paths (Webb et al., 2018), while 1D implementations reproduced the formation of capillary barriers
(Hirashima et al., 2010) and ice lenses (Quéno et al., 2020). Additionally, implementation of capillary forces has been shown
to improve the estimates of snowpack runoff at sub-daily timescales (Wever et al., 2014) as well as reproduce capillary rise on
sea ice (Wever et al., 2020) and at the bottom of the snowpack (Mitterer and Schweizer, 2012).

The implementation of capillary forces in snowpack models is typically done via the Richards equation (Richards, 1931;
Richards and Gardner, 1936), which requires a relationship between the water pressure in the unsaturated porous medium and
liquid water content, called the water retention curve, and the hydraulic conductivity function (Wever et al., 2014; D'Amboise
et al., 2017; Webb et al., 2018; Leroux et al., 2020). These relationships are most commonly described for snow with the
model of Mualem-van Genuchten (Mualem, 1976; van Genuchten, 1980). However, the experimental data needed for deter-
mining the parameter values of the hydraulic functions of this model are rather limited. The water retention curve of snow,
for example, has only been measured directly in limited cases, typically with a vertical resolution on the order of centimeters
~~(Colbeck, 1974, 1975; Wankiewicz, 1976, 1978; Jordan, 1983; Marsh, 1991; Coléou et al., 1999; Yamaguchi et al., 2010, 2012; Adachi et~~
(Colbeck, 1974, 1975; Wankiewicz, 1976, 1978; Jordan, 1983; Marsh, 1991; Coléou et al., 1999; Yamaguchi et al., 2010, 2012; Katsushin
. The most extensive study was performed by Yamaguchi et al. (2012), whose parametrization for the Mualem-van Genuchten
model is the most widely used today and is based on drainage experiments of sieved snow with a vertical resolution of 2 cm.
Due to the relatively large pores in snow, there are large differences between the wetting and drying branches of the water
retention curves (Adachi et al., 2020). The only direct measurements of the wetting branch were by Coléou et al. (1999) and
Adachi et al. (2020), with the experiments by Adachi et al. (2020) having a vertical resolution of 2 mm using magnetic res-
onance imaging (MRI). Other measurements of capillary rise height also exist, but are insufficient for describing the water
retention curve (Coléou and Lesaffre, 1998; Marsh, 1991; Jordan, 1995). In all cases, the measurements of the water retention
curves and capillary rise heights were done in hydrostatic equilibrium without capturing the flow dynamics.

While the water retention curve describes the equilibrium state, the water flow dynamics are controlled by the capillary forces
and the hydraulic conductivity function. Typically, the hydraulic conductivity is measured under saturated conditions and its
dependence on water content is related to the water retention curve. As with the water retention curve data, the data on the satu-
rated hydraulic conductivity of snow are also limited. The saturated hydraulic conductivity of snow has only been directly mea-
sured in a few very limited cases ~~(Katsushima et al., 2013; Clerx et al., 2022)~~(Katsushima et al., 2013; Walter et al., 2013; Clerx et al., 202
. More commonly, the saturated hydraulic conductivity is determined via the permeability, where the conductivity is the prod-
uct of permeability and fluidity (a function of the liquid density and viscosity). The permeability of snow has been measured
(Shimizu, 1970; Jordan et al., 1999; Albert et al., 2000) and also calculated from 3D images of snow microstructure (Courville
et al., 2010; Calonne et al., 2012). The parameterization by Calonne et al. (2012) is the most commonly used method.

When considering the available data above, there are only limited measurements of capillary rise in snow, and, to the best
of our knowledge, none that capture the dynamics. Here, we present the results of 4 capillary rise experiments in snow using
neutron radiography. The experiments provided the 2D evolution of the capillary rise process at a spatial resolution of 92 μm
and temporal resolution of 10 s to 15 s. Motivated by the role of capillary rise in the formation of glide-snow avalanches
(Mitterer and Schweizer, 2012; Lombardo et al., 2025b), the experiments were performed with sand-snow and sand-gravel-
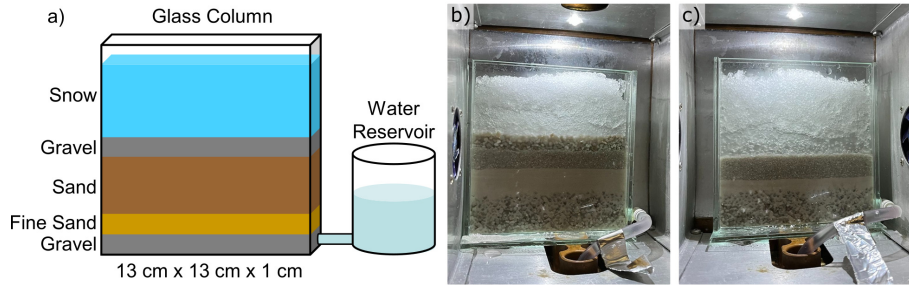
Figure 1. Schematic (a) and photos (b and c) of the column setup. The schematic shows a layering with the transitional gravel layer as does the photo in (b). The photo in (c) is for a layering without gravel. The gravel layer reproduces the effect of the vegetation layer found on grassy slopes. The lower boundary of the column is filled with coarse gravel to facilitate rapid distribution of water from the reservoir.

snow systems, which replicated the capillary forces at the soil-snow interface. The gravel mimicked the weak capillary forces of a vegetation layer found on grassy slopes prone to glide-snow avalanche activity (Feistl et al., 2014; Fees et al., 2025). The results show the effect of the snow and transitional layer properties on the capillary rise process.

2 Materials and methods

2.1 Neutron radiography

Neutron radiography has been shown to be one of the few measurement techniques capable of providing high-resolution, non-destructive measurements of water transport in soil-snow systems and was therefore selected for these experiments (Lombardo et al., 2025c). Neutron radiography experiments were performed on the NEUTRA beamline at the Swiss Spallation Neutron Source (SINQ) of the Paul Scherrer Institute (PSI) in Villigen, Switzerland (Lehmann et al., 2001). Glass columns filled with sand, gravel, and snow were placed inside a climatic chamber within the neutron beam (Mannes et al., 2017). An Andor iKon-L camera using a Zeiss Otus 55 mm f/1.4 lens with a 100 μm ^{6}Li ZnS:Cu scintillator (RC Tritec AG, Teufen, Switzerland) was used as the detector. The resulting pixel size was 92 μm. Images were taken with 10 s or 15 s exposure depending on the experiment with an additional 3 s between exposures for data acquisition by the camera. Vertical bars of perfect neutron absorbers (black bodies made of ^{10}B$_4$C) were placed in front of the climatic chamber and were used for the scattering correction described below.

2.2 Sample preparation

The samples placed into the beam were prepared in glass columns with face dimensions (perpendicular to the beam) of 13 cm × 13 cm with a sample thickness in the beam direction of 1 cm with 3 mm thick walls (Fig. 1a). Each column consisted of a layering of sands (Carlo Bernasconi AG (Bern, Switzerland)) and snow. Sand (0.3–0.9 mm diameter) and gravel (2.0–3.2 mm

diameter) were used as soil and vegetation analogs, respectively. These materials were used to mimic the capillary forces of the soil-vegetation-snow layering found in nature under many gliding snowpacks (Feistl et al., 2014). The gravel was used to

80   mimic the weak capillary forces of a high porosity vegetation layer. Fine sand (0.06–0.25 mm diameter) and gravel were used at the bottom of each column to form a barrier for air infiltration from above after initial wetting, and allow for homogeneous and fast capillary rise into the soil analog layer. The sands and gravel were dry when packing the column. Each column was connected to a water reservoir filled with water at 0 °C with which the height of the water table, and thereby the pressure, was controlled.

85   Two snow types were used. The fine-grained (FG) snow was a natural snow sample of melt forms and small rounded grains with a grain size of 0.25–0.75 mm (Fierz et al., 2009). The coarse-grained (CG) snow was an artificial snow sample grown using the Snowmaker (Schleef et al., 2014) and stored at 0 °C with periods at +2 °C in the laboratory to generate melt forms with grain size 0.5–1.5 mm (Fierz et al., 2009). The fine-grained snow had a density of 531 kg m^{-3} and coarse-grained snow had a density of 547 kg m^{-3} as determined from micro-computed tomography (μCT) scans (Fig. A1). The densities were

90   expected to vary from the laboratory values after packing into the column at PSI. Specific surface area (SSA, surface area per mass snow) was also determined from the μCT scans and was used to calculate the optically equivalent grain size needed for the parameterization described by Calonne et al. (2012). The optically equivalent grain diameter was determined using the relationship $d = 6 \times SSA^{-1} \times \rho^{-1}$ (Calonne et al., 2012). Micro-computed tomography was performed on a μCT 90 by SCANCO Medical AG (Brüttisellen, Switzerland) with a voxel size of 11 μm, and X-ray tube settings of 55 kVp and 8 W. The

95   segmentation was performed using the method described by Hagenmuller et al. (2013).

A total of 4 samples were prepared. Two configurations (FG$_{s,g}$ and CG$_{s,g}$) had a gravel layer between the sand and the snow (Fig. 1b), while the other two (FG$_s$ and CG$_s$) had snow directly in contact with the sand (Fig. 1c). The configurations are notated with FG or CG for the snow type, with the subscript "s" denoting the sand-snow layering and "s,g" denoting the sand-gravel-snow layering.

2.3   Capillary rise experiment procedure

The sand and gravel layers were dry packed into the column at room temperature, after which the column was placed into an ice bath at 0 °C. During this time, the necessary neutron images (open beam and dark current, see below) without the column were acquired prior to the experiment. Once the column reached 0 °C, snow stored at -15 °C to -20 °C was transferred into the column with a spatula. The sintered snow in the storage container was broken with the spatula and poured/spooned into

105   the container as loose grains. The column remained in the ice bath during snow packing while the ambient air temperature was room temperature (approximately 20-25 °C). The column was transferred to the climate chamber (-5 °C) in the ice bath, minimizing the time at room temperature. When the column was in the chamber, a hose was routed through the bottom of the chamber and connected to the reservoir filled with ice water. The water level was set to 1 cm below the top of the sand (soil analog) accounting for the water level loss due to the volume of water in the tubing. The hydraulic head therefore reduced

110   slightly (approximately 0.5 cm) during the filling of the tubing and column, but is assumed to have a minimal effect on the dynamics. The chamber temperature was then set to 0 °C for the duration of the experiment. The experiment was started by

opening a valve allowing for water to flow from the reservoir into the column. Due to the safety requirements of the beamline, there was always a delay between the opening of the valve and the first image. This is why the region of interest in the first images are not completely dry and, in some experiments, the water was already within the snow by the time the first image was taken (e.g., FG_s). This procedural limitation has several implications on the analysis, which are discussed in more detail below.

2.4 Image processing

Image processing was performed using Python 3.8 with standard Python libraries. Image processing was necessary to correct the raw images for various effects such as dark-current (detector signal while the neutron beam is off), attenuation from the non-sample components such as the climate chamber, neutron scattering effects of the sample and non-sample components, and fluctuations of the neutron beam. The corrections were performed following the method described by Lombardo et al. (2025c) to obtain the unitless optical density (OD)

$$OD_\mathrm{n} = -\ln\left(\frac{I_\mathrm{n,BB} - I_\mathrm{DC} - I^\mathrm{S}_\mathrm{n,BB}}{I_\mathrm{OB,BB} - I_\mathrm{DC} - I^\mathrm{S}_\mathrm{OB,BB}} \cdot \frac{D^\mathrm{p}_\mathrm{OB,BB}}{D^\mathrm{p}_\mathrm{n,BB}} \right) \tag{1}$$

where OD_n is the optical density of the nth sample image, $I_\mathrm{n,BB}$ is the measured intensity of the nth image with black bodies, I_DC is the dark-current, $I_\mathrm{OB,BB}$ is the open-beam image (empty climate chamber) with black-body bars, $I^\mathrm{S}_\mathrm{n,BB}$ is the scattering contribution of the nth image with black-body bars, $I^\mathrm{S}_\mathrm{OB,BB}$ is the scattering contribution of the open-beam image with black-body bars, $D^\mathrm{p}_\mathrm{OB,BB}$ is the proton dosis of the open-beam images with black-body bars, and $D^\mathrm{p}_\mathrm{n,BB}$ is the proton dosis of the nth image with black-body bars. The proton dosis terms correspond to the proton current at the neutron generating target and are proportional to the neutron flux.

One improvement to the method by Lombardo et al. (2025c) was the use of continuous vertical black-body bars instead of a grid of black-body cylinders to improve the vertical resolution of the scattering correction. Virtual black bodies were created along each black-body bar to replicate the cylinder grid configuration, but with a higher vertical resolution. 20 evenly-spaced virtual black bodies were placed on each bar (Fig. 2). The black-body values were calculated as the mean of an 11 pixel $\times$ 11 pixel square around each virtual black-body location. This resulted in one intensity value per virtual black body, which was subsequently used for the thin-plate spline interpolation to obtain the scattering images ($I^\mathrm{S}_\mathrm{n,BB}$ and $I^\mathrm{S}_\mathrm{OB,BB}$) (Carminati et al., 2019; Lombardo et al., 2025c). Due to significant amount of scattering from the water and ice, a beam hardening correction was applied to the scattering-corrected optical density using the polynomial expression ($y = 0.99x + 0.03x^2 + 0.0009x^3$) reported by Carminati et al. (2019) for the NEUTRA beamline, where x is the calculated optical density from Eq. 1 and y is the optical density after the beam-hardening correction. Finally, the optical density of the glass column walls (0.192 ± 0.009) was subtracted from the beam-hardening corrected optical density. The glass value was experimentally determined using the same method described above for an empty column. The value was assumed to be the same for all columns.

The correction method was validated by measuring the linear attenuation coefficient of water and comparing it to the value of 3.6 cm^{-1} reported by Carminati et al. (2019). The linear attenuation coefficient is related to the optical density through
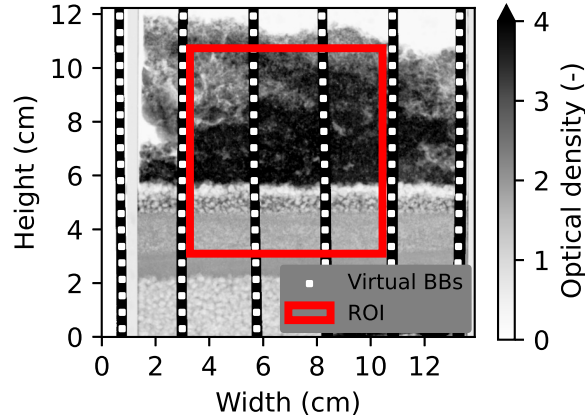
Figure 2. An example of an optical density image showing the region of interest (ROI) used for the calculations (red box). The black bodies are the vertical black bars and the virtual black bodies (BBs, white rectangles) were placed within the black bodies at even intervals.

$$OD = \mu z \tag{2}$$

where OD is the unitless optical density, μ is the linear attenuation coefficient in cm^{-1}, and z is the path length in cm. The linear attenuation coefficient of water was measured with an aluminum wedge with steps of different water thicknesses in the beam direction (path lengths) between 0.5 mm and 5 mm. Applied to the wedge, the correction method resulted in a linear attenuation coefficient for water of 3.60 ± 0.02 cm^{-1} (Fig. 3), which matches the value of 3.6 cm^{-1} reported by Carminati et al. (2019).

2.5 Liquid water content

Liquid water content~~in~~, expressed as volume of water per total sample volume, of snow was derived from the optical density through the following relationships. First, the total optical density can be expressed as the sum of optical densities of the sample components (ice and water) as

$$OD_{\text{total}} = OD_{\text{ice}} + OD_{\text{water}} \tag{3}$$
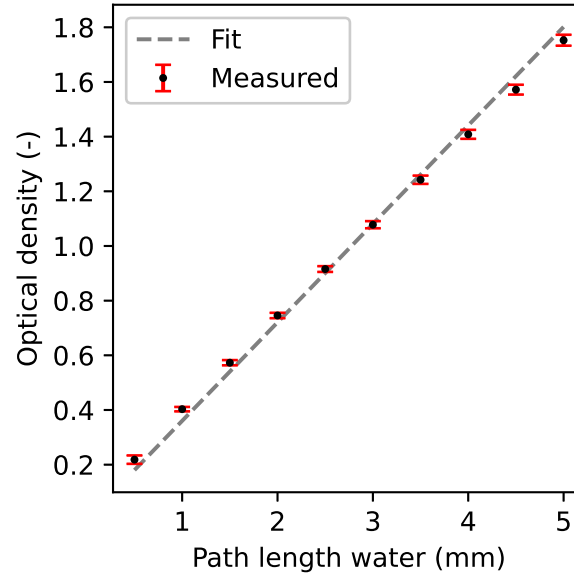
Figure 3. The measured optical density of the reference (aluminum wedge with varying water thicknesses) as a function of water thickness or path length (black dots) with error bars of the standard deviation (red) and linear fit (dotted gray line). Fit equation: $OD = 0.360(\pm 0.002)z$, where z is the path length in mm and OD is the unitless optical density. The slope of 0.36 mm^{-1} (or 3.6 cm^{-1}) is the expected attenuation coefficient of water.

where OD_{total} is the total optical density, OD_{ice} is the optical density of the ice, and OD_{water} is the optical density of the
155 water. The optical density of air is negligible and the contribution of the glass was already subtracted (as explained above). Then, since optical density is the product of the linear attenuation coefficient (μ) and path length (z), Eq. 3 can be rewritten as

$$OD_{\text{total}} = \mu_{\text{ice}} z_{\text{ice}} + \mu_{\text{water}} z_{\text{water}} \tag{4}$$

where the linear attenuation coefficients and path lengths are given for ice and water. Using the measured value for μ_{water} of 3.60 ± 0.02 cm^{-1}, the linear attenuation of ice is calculated as

160 $$\mu_{\text{ice}} = \mu_{\text{water}} \frac{\rho_{\text{ice}}}{\rho_{\text{water}}} \tag{5}$$

resulting in a value of 3.26 ± 0.02 cm^{-1} when ρ_{water}=1000 kg m^{-3} and ρ_{ice}=917 kg m^{-3}. This assumes that the only difference in attenuation between ice and water is the density. While the linear attenuation coefficient is also a function of neutron energy, the energy-related differences between ice and water are negligible for the thermal neutron energy spectrum (mean energy of 25 meV) of the NEUTRA beamline (Lehmann et al., 2001). Now, the path lengths of ice and water (z_{ice} and z_{water}) can be

expressed as fractions of the total path length (z), which are simply the ice volume fraction and volumetric liquid water content (θ) for ice and water, respectively. Thus, Eq. 4 can be rewritten as

$$OD_{\text{total}} = \mu_{\text{ice}} \frac{\rho_{\text{snow,dry}}}{\rho_{\text{ice}}} z_{\text{total}} + \mu_{\text{water}} \theta z_{\text{total}} \tag{6}$$

where $\rho_{\text{snow,dry}}$ is the dry snow density, θ is the volumetric liquid water content (given as a fraction) of the snow, and z_{total} is the total path length of the column (here, 1 cm). Reorganization of Eq. 6 provides an expression for snow liquid water content

$$\theta = \frac{1}{\mu_{\text{water}}} \left(\frac{OD_{\text{total}}}{z_{\text{total}}} - \mu_{\text{ice}} \frac{\rho_{\text{snow,dry}}}{\rho_{\text{ice}}} \right) \tag{7}$$

where all quantities are known or measured except for $\rho_{\text{snow,dry}}$. Since the linear attenuation coefficients between ice and water only differ due to the difference in their densities for the NEUTRA energy spectrum, we cannot directly distinguish between ice and water when the corresponding path lengths are unknown. Thus, when calculating the liquid water content, the dry snow density must be known (described in the next section).

2.6 Dry snow density

The dry snow density ($\rho_{\text{snow,dry}}$) was calculated as

$$\rho_{\text{snow,dry}} = \frac{OD_{\text{dry}}}{\mu_{\text{ice}} z_{\text{total}}} \rho_{\text{ice}} \tag{8}$$

where OD_{dry} is the optical density of the snow in a dry state and the other variables are defined above. This assumes that 1) the dry state was truly dry and 2) no changes to the snow occurred during the experiment (e.g., densification). The dry state was always determined from the first image. For the horizontally averaged vertical profiles, the average optical density of a manually selected vertical region of the sample (e.g., from 0.5 cm to 2 cm above the bottom of the snow layer) was taken as the dry snow density. Thus, a single dry snow density was used for the entire vertical profile. This manual selection was necessary because $CG_{\text{s,g}}$, CG_{s}, and FG_{s} already had some water present within the snow in the first image. The dry snow density used for the vertical profiles is provided in Tab. 1. For the analysis of the 2D images, the dry state was defined on a per-pixel basis, where the dry snow density was calculated from the first image, regardless of the presence of water. The implications of these assumptions are addressed in the Discussion section.

2.7 Flow rates

The flow rate of water from the sand or gravel into the snow was calculated from the horizontally averaged liquid water content profiles as

$$q = \frac{\Delta \theta}{\Delta t} H \tag{9}$$

where q is the flow rate in cm min^{-1}, $\Delta\theta$ is the change in liquid water content of the snow between two images, Δt is the change in time (min) between the two images, and H is the height (cm) of the snow within the ROI. For this calculation, the flow was assumed to be only vertical. The horizontal averaging of the liquid water content profiles was done for each pixel height. The results were smoothed with a Savitzky-Golay filter (Savitzky and Golay, 1964) with a window length of 10 and a third order polynomial to reduce the noise of the signal and make the curves more legible.

2.8 Water retention curve fitting

The water retention curve describes the relationship between capillary pressure and liquid water content. Here, we used the van Genuchten model (van Genuchten, 1980) given by

$$\theta\left(h\right) = \theta_{\mathrm{r}} + \frac{(\theta_{\mathrm{s}} - \theta_{\mathrm{r}})}{[1 + (\alpha h)^{n}]^{m}} \tag{10}$$

where h is pressure head or matric potential head (expressed here as the absolute value of the negative head or height above the water table), θ is volumetric liquid water content, θ_{r} is residual liquid water content, θ_{s} is saturated liquid water content, and three parameters: α, n, and m. While θ_{r} and θ_{s} have direct physical meanings as the minimum and maximum amount of water, n and α are related to the width of pore-size distribution and the inverse of the air-entry pressure, respectively (van Lier and Pinheiro, 2018).

Fitting of the water retention curves was performed on the horizontally averaged liquid water content profiles from the last image of each experiment, which assumes that the water distribution is close to hydrostatic equilibrium. An example fit of FG$_{\mathrm{s,g}}$ is provided in Fig. 4 with the remaining fits in the Appendix (Fig. A5, Fig. A6, Fig. A7). The pressures were calculated based on the height above the water level in the reservoir. The fit was performed using a nonlinear least squares approach with Eq. 10. All parameters were allowed to vary freely except θ_{r}, which was limited to a value close to zero (maximum 0.001). Typically, a value of around 0.02 is used for the residual water content of snow (Yamaguchi et al., 2012; Wever et al., 2014). However, since the initial wetting curve of a truly dry sample cannot start at a value greater than 0, a value of 0 was more appropriate for these experiments. The relationship $m = 1 - 1/n$ was used (van Genuchten, 1980), where n must be larger than 1.

The mean absolute error (MAE) was used to quantify the quality of the fitting as

$$MAE = \frac{1}{n_{\mathrm{m}}} \sum |y_{\mathrm{measured}} - y_{\mathrm{fit}}| \tag{11}$$

where n_{m} is the number of measurements, y_{measured} are the measured values, and y_{fit} are the fit values. The measured values were the horizontally averaged liquid water content values measured by neutron radiography and the fit values were from the least squares regression. The units of the MAE are liquid water content expressed as volume fraction.
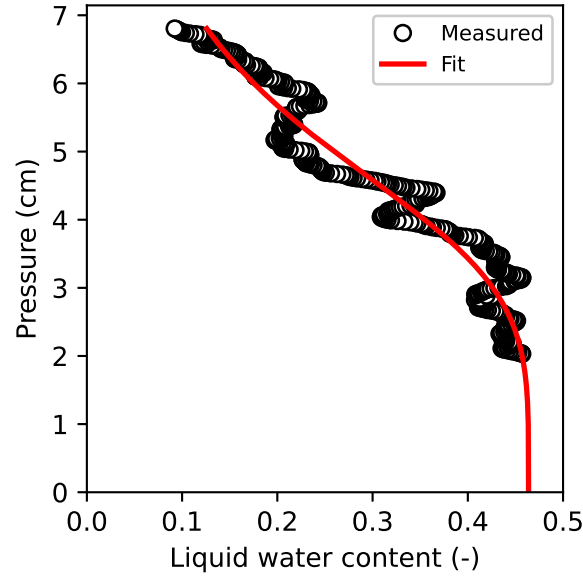
Figure 4. The 1D liquid water content of $FG_{s,g}$ as a function of pressure head (black circles) and the fit of these points to Eq. 10 (red line) with ~~R^2=0.95~~ mean absolute error equal to 0.022 and expressed as the volume fraction of liquid water content.

2.9 Hydraulic conductivity fitting

220   Fitting of the hydraulic conductivity was performed using the inverse solution method of Hydrus-1D on the measured capillary rise data (Šimůnek et al., 2008). The fit was performed on the Mualem-van Genuchten function (Mualem, 1976; van Genuchten, 1980) which combines Eq. 10 with

$$K\left(S_{\mathrm{e}}\right) = K_{\mathrm{s}} S_{\mathrm{e}}^{\frac{1}{2}} \left[1 - \left(1 - S_{\mathrm{e}}^{\frac{1}{m}}\right)^{m}\right]^{2} \tag{12}$$

where K_{s} is the hydraulic conductivity at saturation, m is again taken as $1 - 1/n$, and S_{e} is the effective saturation defined as

225   $$S_{\mathrm{e}} = \frac{\theta\left(h\right) - \theta_{\mathrm{r}}}{\theta_{\mathrm{s}} - \theta_{\mathrm{r}}} \tag{13}$$

which accounts for the pore volume occupied by the residual water. The exponent of 1/2 is the default value of the τ parameter, which describes the effects of the connectivity and tortuosity of the flow paths. This parameter was not fit in this study (see Discussion). An example fit of $FG_{s,g}$ is provided in Fig. 5 with the remaining fits in the Appendix (Fig. A8, Fig. A9, Fig. A10).

The simulations included 5 cm of snow and 0.5 cm of a transitional layer below the snow with a total of 221 ~~nodes. This~~

230   numerical nodes (spatial resolution of 0.025 cm). The transitional layer captured the upper part of the gravel layer for $FG_{s,g}$ and $CG_{s,g}$, the sand for FG_{s} and CG_{s}, and the gravel-snow or sand-snow interface, respectively. The snow layers were initialized

using the liquid water content profile within the snow (calculated with Eq. 6 and Eq. 8). The transitional layer was initialized in a dry state (pressure $\leq$ 50 cm) with the pressure of the lowest node set to the height above the water level in the reservoir. The simulation began at t=0.

235   The upper boundary condition was a constant zero flux condition and the lower boundary condition was a constant pressure head based on the distance of the lower boundary to the height of the water level in the reservoir. Fitting was performed to 10 ~~observation nodes at~~ numerical nodes (called "observation nodes" in Hydrus) that act as virtual sensors to record the liquid water content. The observation nodes had a vertical spacing of 0.5 cm ~~spacing~~ and fitting was performed at 11 timesteps. The parameters θ_r, θ_s, α, n of the snow were fixed to the values obtained by the water retention curve fitting and the saturated

240   hydraulic conductivity was allowed to vary. For $CG_{s,g}$, the static fitting resulted in a value of n=18.6, which made the inverse fitting difficult, as a high n value leads to large changes in LWC for small changes in pressure. This prohibited the model from converging and a smaller value of 10 was needed to perform the fitting for this experiment. The transition layers in $FG_{s,g}$ and $CG_{s,g}$ were described with arbitrary values for θ_r, θ_s, α, and n of 0.00, 0.43, 0.5 cm^{-1}, and 3.0, respectively, such that the layer remained relatively dry (see Results). The θ_r, θ_s, α, n values for the transitional layers in FG_s and CG_s were 0.04, 0.38,

245   0.06 cm^{-1}, and 8.1, respectively, which are the values fit to the water retention curve from drainage experiments measured in the lab for the sand (Lombardo et al., 2025c). The saturated hydraulic conductivity of the transitional layer was also fit. The MAE (Eq. 11) was calculated in the same way as for the water retention curves described above with the measured values coming from the (horizontally averaged) neutron radiography experiments and the fit values coming from the inverse fitting. The Hydrus files for each of the simulations are provided by Lombardo et al. (2025a).

250   ## 2.10   Wetting front tracking

The wetting front was defined as the region of 50% saturation, where saturation is defined as the fraction of the pore space ~~. Since the residual watercontent was fixed to 0 and the saturated~~ filled with water. The saturation (S) was calculated using the relationship

$$\theta = \left(1 - \frac{\rho_{\text{snow,dry}}}{\rho_{\text{ice}}}\right) S \tag{14}$$

255   where $1 - \frac{\rho_{\text{snow,dry}}}{\rho_{\text{ice}}}$ is the porosity, θ is the liquid water content ~~was equal to the pore space, this is equivalent to the effective saturation defined by van Genuchten (1980)~~ calculated from Eq. 7, $\rho_{\text{snow,dry}}$ is the dry snow density calculated with Eq. 8, and ρ_{ice} is the density of ice (917 kg m^{-3}). The wetting front was tracked individually for each of the three regions separated by the black-body bars, called Left, Middle, and Right (Fig. 9). The ~~optical density image was converted to saturation using Eq. 8 and the relationship~~

$$\theta = \left(1 - \frac{\rho_{\text{snow,dry}}}{\rho_{\text{ice}}}\right) S$$
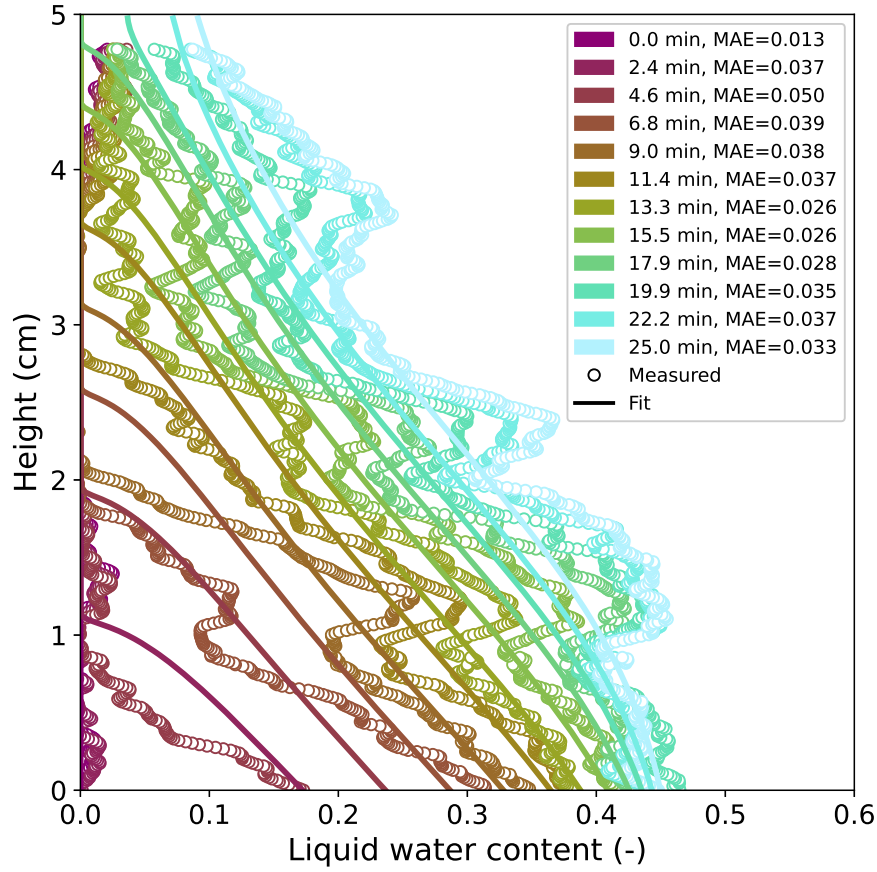
Figure 5. The temporal evolution of the vertical liquid water content profile (circles) of $FG_{s,g}$ and the accompanying results of the inverse fitting (lines) with mean absolute error (MAE) expressed as the volume fraction of liquid water content.

~~where $1 - \frac{\rho_{\text{snow,dry}}}{\rho_{\text{ice}}}$ is the porosity and S is the volumetric fraction of the pore space filled with water, also known as saturation and usually differs from the effective saturation S_{e} defined above. The~~ dry density was calculated ~~separately~~ for each pixel from the first image as described above. The saturation image (for each region) was filtered using a Gaussian filter (σ=2). The filtered image was then segmented using a saturation threshold of 50% (inclusive). Object labeling was performed and objects smaller than 700 pixels were removed to focus on the upward moving front and to eliminate small regions of high liquid water content which were more likely to be artifacts. The maximum height of all pixels in the segmented image was then used as the wetting front position. This height was added to the pressure head (in cm) at the bottom of the snow to provide the position with respect to the water table.
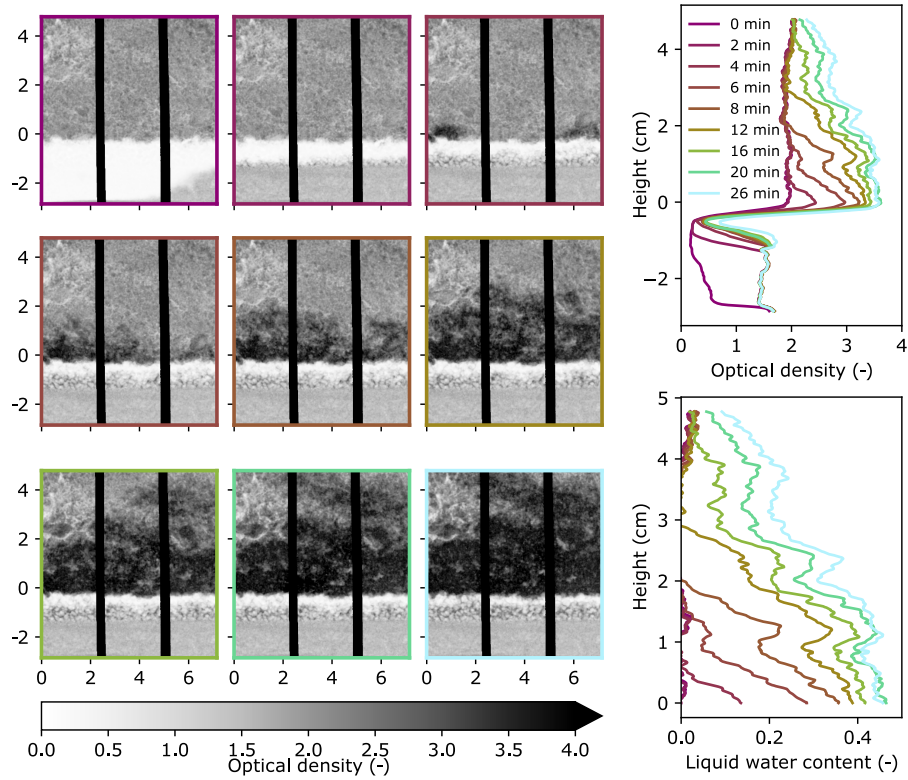
Figure 6. Summary figure of experiment $FG_{s,g}$ showing the 2D optical density evolution over time (left), 1D horizontally averaged optical density profile evolution over time (top right), and 1D horizontally averaged liquid water content profile of the snow over time (bottom right). The 2D images correspond to the times in the vertical profiles (right) as indicated by the color. The units for the optical density images (left) are cm for both axes. For the y-axes of all plots in this figure, a height of 0 cm was defined as the height where the continuous snow phase begins, where the effects of the gravel-snow interface are no longer present. The vertical black-body bars are shown in black in the images (left).

3 Results

270 Each of the 4 capillary rise experiments resulted in a time series of 2D optical density images, which were used to obtain 1D and 2D information about the capillary rise process. An overview of $FG_{s,g}$ is provided in Fig. 6 and the corresponding overview plots for the other experiments are in the Appendix (Fig. A2–Fig. A4). The overview figures show the relationship between the 2D evolution of the optical density over time and the 1D profiles (optical density and liquid water content). Specifically, regions of higher optical density (vertically) in the 2D images correspond to regions with more water (and/or ice) and these

275 regions have increased optical density and liquid water content in the 1D profiles.

When analyzing all 4 experiments, a few general results become clear. First, the 2D images show that the capillary rise process was not spatially homogeneous (Fig. 7). Second, the fine-grained snow led to higher capillary rise heights compared
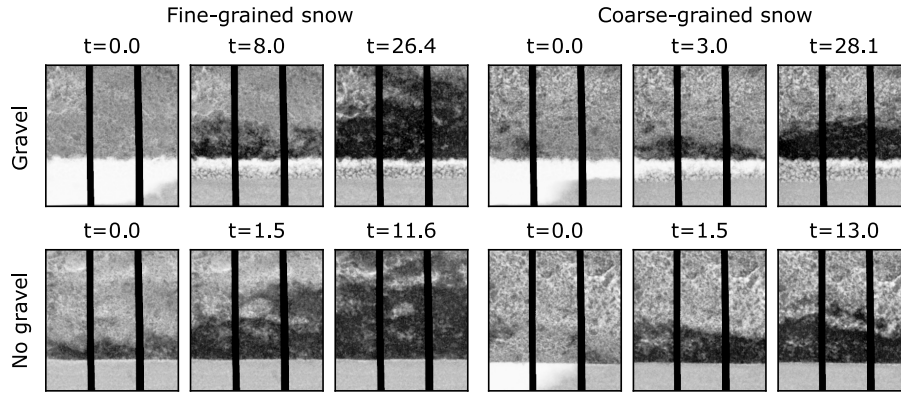
Figure 7. A summary of the 4 experiments showing the 2D optical density images at 3 times (t) given in minutes. The experiments are classified based on their snow type and whether or not they included a gravel layer. These correspond to $FG_{s,g}$ (top left), FG_s (bottom left), $CG_{s,g}$ (top right), and CG_s (bottom right). The vertical black-body bars are shown in black.

to the coarse-grained snow. Finally, the 1D optical density profiles show that the rate of capillary rise was higher for the experiments without the porous gravel layer (Fig. 8). Thus, the properties of both the snow and the transitional layer below the snow influenced the capillary rise process.

3.1 Spatio-temporal variability

The 2D spatio-temporal variability of the capillary rise process was assessed by tracking the wetting front. An example of the wetting front progression is provided for $FG_{s,g}$ in Fig. 9, which shows the spatial and temporal inhomogeneity of the capillary rise process. The image is separated into three regions based on the black bodies. For $FG_{s,g}$, the water first rose in the left region (labeled as 1 in Fig. 9), but to a lower final height compared to the middle and right regions. In addition to the upwards flow direction, the figure also shows lateral flow patterns. For example, water flowed from the right region into the middle region from 15 min to 20 min, between 3 cm and 4 cm (labeled as 2 in Fig. 9). At the end of the experiment, the three regions showed different wetting front patterns.

Some of the spatio-temporal variability is likely related to variations in snow properties. For example, regions of $FG_{s,g}$ that remained less saturated were characterized by particularly low densities with larger pores and weaker capillary forces (Fig. 10). Additionally, the fine-grained snow led to higher final wetting front positions (7 cm to 8 cm) compared to the coarse-grained snow (4 cm to 5 cm) as seen in Fig. 8 and Fig. 11. It should be noted that the wetting fronts in both experiments with the fine-grained snow ($FG_{s,g}$ and FG_s) reached the top of the image, so the maximum capillary rise heights are unknown. There were also differences in the final wetting front heights for each of the three image regions, on the order of 0.5 to 1.5 cm. Differences in the wetting front position during the experiments were larger, up to several centimeters. The wetting fronts tended to progress in sudden, relatively large increases as opposed to a smooth progression. Overall, $FG_{s,g}$ took the longest to reach its final wetting front position ($\sim$15 min–20 min depending on the region), while the other experiments reached their
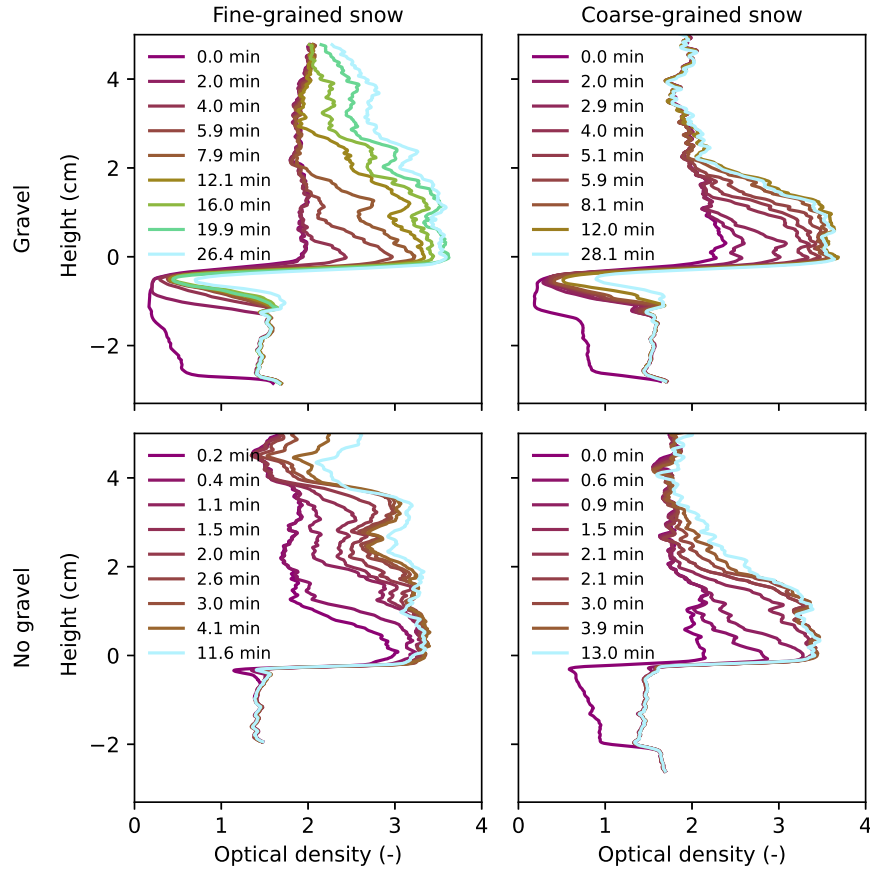
Figure 8. A summary of the 4 experiments showing the 1D optical density profiles at 9 times. The experiments are shown based on their snow type and whether or not they included a gravel layer. These correspond to $FG_{s,g}$ (top left), FG_s (bottom left), $CG_{s,g}$ (top right), and CC_s (bottom right). The unsaturated gravel layer can be seen in the upper plots as the reduction in optical density below a height of 0 cm.

final positions in approximately 5 min. The wetting front tracking also highlighted the presence of water in the initial image (e.g., black circles in $CG_{s,g}$ in Fig. 11).

3.2 Flow rates

While the snow properties affected the capillary rise height, the properties of the transition layer under the snow affected the flow rates (Fig. 12). The experiments without the gravel layer (FG_s and CG_s) exhibited higher maximum flow rates compared to the experiments with the gravel layer ($FG_{s,g}$ and $CG_{s,g}$). These calculated flow rates are roughly an order of magnitude lower than the saturated hydraulic conductivities determined via the inverse fitting (described in detail below), which is related to the unsaturated conditions in the transition layer. Additionally, the flow rates tended to drop to zero a few minutes after the wetting fronts reached their final position. For $FG_{s,g}$, the flow rates dropped to zero after 20 min, while this drop occurred between 5
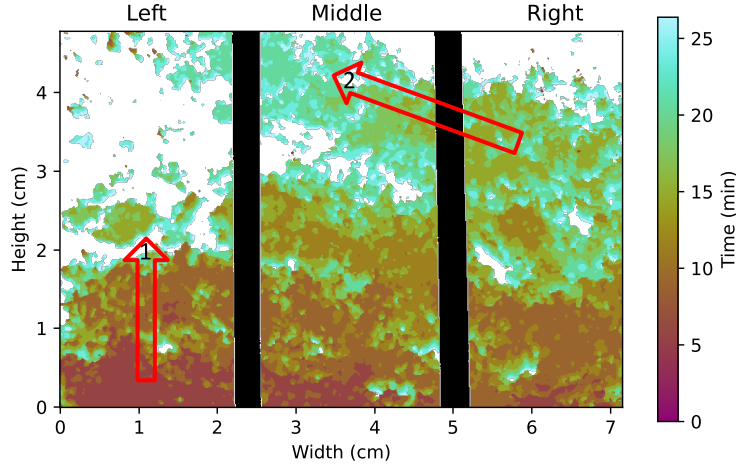
Figure 9. 2D wetting front evolution for fine-grained snow with gravel layer ($FG_{s,g}$). The times in the colorbar indicate when 50% saturation was achieved. White regions never reached 50% saturation. The black columns indicate the positions of the black-body bars. Key movements are labeled with red arrows (1) initial infiltration in the Left region and (2) horizontal flow from the Right to the Middle region

min and 10 min for the other three experiments. This demonstrates that regions behind the wetting front continue to gain water after the front has passed.

3.3 Fitting hydraulic parameter values

310 The results of the fitting of the water retention curve (~~e.g.~~ Fig. 4, Fig. A5–Fig. A7) and inverse (~~e.g. fitting of temporal~~ dynamics (Fig. 5~~) fitting~~, Fig. A8–Fig. A10) are provided in Tab. 1 with comparison to literature values using standard methods for determining these parameters. The ~~fitted~~ MAE for the static fits ranged from 0.019–0.041 liquid water content (Fig. 4, Fig. A5–Fig. A7). The MAE for the inverse fits ranged from 0.013–0.076 liquid water content and was calculated for each timestep (Fig. 5, Fig. A8–Fig. A10).

315 The fit saturated liquid water content values (θ_s) varied less than 10% from those estimated ~~with densities~~ based on the optical density and μCT scans. The α parameters for the experiments with the fine-grained snow (FG_s and $FG_{s,g}$) resulted in similar values of 0.21 cm^{-1} and 0.19 cm^{-1}, respectively. The α values for the experiments with the coarse-grained snow (CG_s and $CG_{s,g}$) varied more at 0.22 cm^{-1} and 0.30 cm^{-1}, respectively. The n values followed the same pattern with lower and similar n values of 4.5 and 3.5 for the experiments with fine-grained snow (FG_s and $FG_{s,g}$), with larger and more dissimilar n values of 18.6

320 and 7.3 for experiments with the coarse-grained snow (FG_s and $FG_{s,g}$), respectively. The van Genuchten parameters resulting from the water retention curve fitting significantly differed from the values obtained with the parameterization by Yamaguchi et al. (2012). The α values obtained by the fitting were approximately 2–4 times larger than parameterized values when using
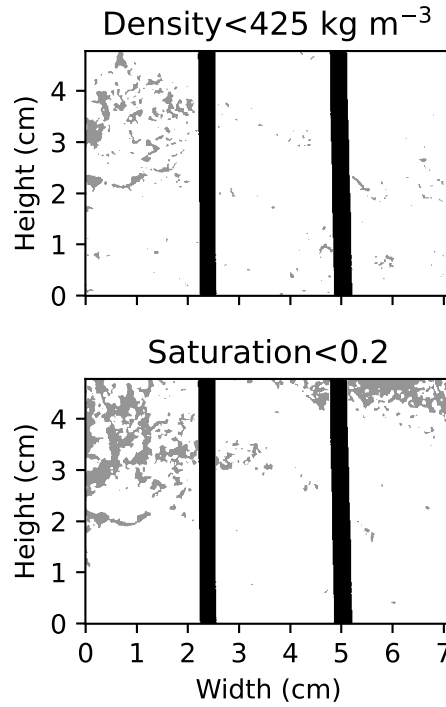
Figure 10. Segmented images of FG$_{s,g}$ showing regions with dry densities less than 425 kg m^{-3} in gray (top image) and regions with final saturation values less than 20% in gray (bottom image). The black bodies are shown in black. The region of low saturation in the upper right of the saturation plot is an artifact of high initial density due to surface melting, which caused a high initial density and therefore a small increase in saturation.

the grain diameter visually estimated using a crystal card grid. Conversely, the n values obtained via the parameterization by Yamaguchi et al. (2012) were 1-4 times larger than those obtained by fitting. The smaller n values obtained via fitting correspond to a wider pore size distribution compared to the parameterization.

Similarly, the saturated hydraulic conductivity (K_s) values for the snow predicted by the parameterization of Calonne et al. (2012) were 1-6 times larger than the values obtained by the inverse fitting. There was no clear difference between the fine-grained and coarse-grained snow. The fitting resulted in K_s values for the transitional gravel layer of 0.33 cm min^{-1} and 3.41 cm min^{-1} for FG$_{s,g}$ and CG$_{s,g}$, respectively. Fitting of FG$_s$ and CG$_s$ resulted in K_s values for the transitional sand layer of 0.16 cm min^{-1} and 0.15 cm min^{-1}, respectively. As discussed in the following section, these values reproduce the complexities of the hydraulic conductivity function of the transitional layer.
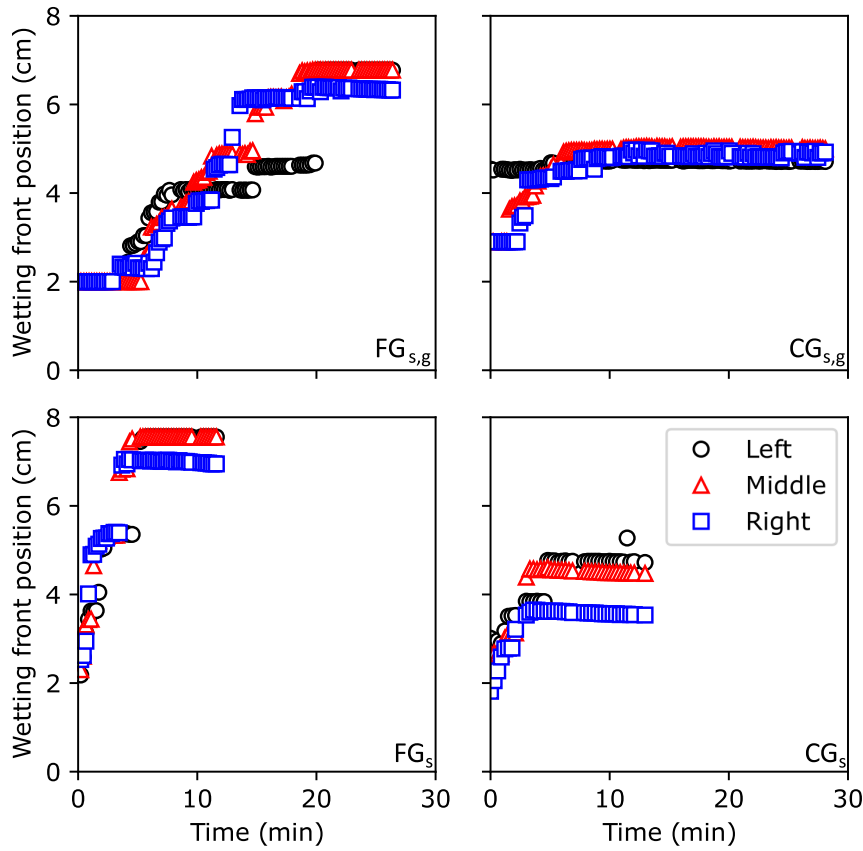
Figure 11. The progression of the wetting fronts for the three regions between each black-body for each experiment. The wetting front position is provided with respect to the water table. The legend in CG$_s$ applies to all plots in the figure.

4 Discussion

Neutron radiography was used to image the capillary rise of water from sand and gravel into snow. The images showed the 2D evolution of the liquid water distribution and fitting allowed for quantification of hydraulic parameter values of the van Genuchten model and saturated hydraulic conductivity. The parameter values were compared to literature values.

4.1 Flow rates

The flow rate of water into the snow was predominantly influenced by the transitional layer below the snow. As seen in Fig. 12, the presence of the unsaturated transitional gravel layer below the snow led to reduced flow rates compared to the configurations with only the sand. This is because the hydraulic conductivity of a material increases with saturation in a highly non-linear way (Eq. 12). Since the transitional gravel layers were relatively dry while the transitional sand layers were relatively wet, the
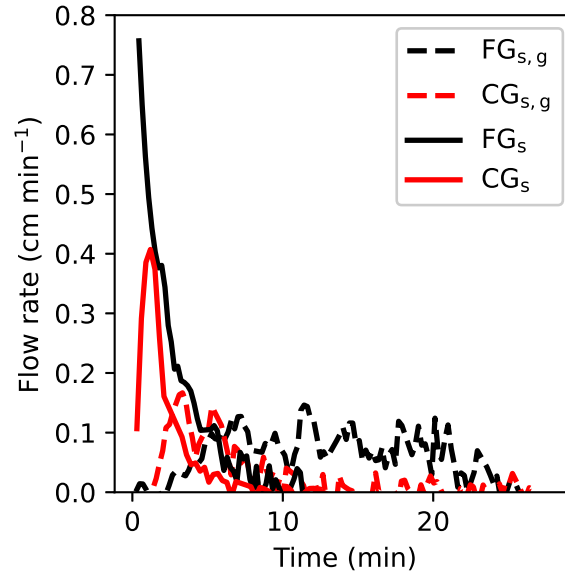
Figure 12. Flow rates of water into the snow for each experiment deduced from the images and calculated based on Eq. 9. The dashed lines represent the experiments with the interfacial gravel layer.

Table 1. Parameter values determined in this study and comparison values from the literature

Experiment	Measured snow properties				Fitted parameters[g]					Comparison values		
	ρ_{OD}[a]	$\rho_{\mu CT}$[b]	$d_{\mu CT}$[c]	d_{CC}[d]	θ_r	θ_s	α	n	K_s	α[e]	n[e]	K_s[f]
—	kg m^{-3}	kg m^{-3}	mm	mm	–	–	cm^{-1}	–	cm min^{-1}	cm^{-1}	–	cm min^{-1}
FG$_{s,g}$	540	531	0.5	0.5	0.00	0.46 (0.005)	0.21 (0.004)	4.5 (0.3)	3.3 (0.7)	0.054	14.0	5.5
FG$_s$	502	531	0.5	0.5	0.00	0.43 (0.01)	0.19 (0.01)	3.5 (0.5)	2.9 (0.3)	0.058	13.4	9.1
CG$_{s,g}$	560	547	0.8	1.0	0.00	0.43 (0.003)	0.22 (0.0005)	18.6 (0.6)	1.7 (0.4)	0.102	9.7	10.9
CG$_s$	487	547	0.8	1.0	0.00	0.46 (0.003)	0.30 (0.001)	7.3 (0.2)	18.0 (3.9)	0.118	9.0	28.2

[a] Density calculated from the neutron images

[b] Density calculated from the μCT scans

[c] Optically equivalent diameter based on the SSA from the μCT scans

[d] Average grain size using crystal card grid

[e] Based on Yamaguchi et al. (2012) using d_{CC}

[f] Based on Calonne et al. (2012) using $d_{\mu CT}$

[g] Standard error provided in parenthesis for K_s and standard deviation for the static fit parameters

hydraulic conductivity of the transitional gravel layer was lower. The flow rates did not show any distinction with respect to the snow properties.

The flow rates were also significantly lower (1–2 orders of magnitude) than the saturated hydraulic conductivity values of the snow (inverse fitting and parameterized) and sand (Lehmann et al., 2008). This was likely due to a combination of factors. First, the sand and gravel were packed dry, which led to incomplete saturation. For example, the sand reached a saturation between 76% and 82% when using the apparent density provided by the manufacturer to calculate the dry porosity. No value could be calculated for FG_s because the sand was already wet in the first image. As mentioned above, since hydraulic conductivity increases with saturation, this resulted in lower flow rates than if the sand were perfectly saturated. Second, the imperfect gravel-snow and sand-snow interfaces were likely more porous than either the gravel or sand themselves, respectively, resulting in slower forms of flow such as corner and film flow compared to flow through saturated pore bodies. Finally, the flow was influenced by the pressure gradient. During infiltration, regions of the sample below the water level experienced a positive pressure head (upward force) while regions above the water level experienced a negative pressure head (downward force).

4.2 Fitted values - water retention curve fitting

The MAE of the water retention curve fitting varied from 0.019–0.041 liquid water content, with FG_s having the highest MAE of 0.041 and the remaining experiments having similar MAEs of 0.019–0.023. The MAE can be used in combination with the standard deviation of the fit values (Tab. 1) to assess the overall quality of the fit as well as the confidence in the individual fit parameters. For example, the largest standard deviations for the α and n parameters were obtained in the fit for FG_s, which also had the largest MAE. Additionally, for $FG_{s,g}$, CG_s, and $CG_{s,g}$, a standard deviation in the α parameter of up to 2% and a standard deviation in the n of up to 7% led to an MAE of about 0.02. An MAE of 0.02 is similar to the errors of 2%–5% reported for high-resolution liquid water content measurement techniques such as calorimetry and MRI (Adachi et al., 2020), while Barella et al. (2024) reported a much higher accuracy of 0.5% for calorimetry. Thus, the fitting itself has an MAE that is similar to the error of the best measurement techniques and, considering the limitations and assumptions (e.g. 1D, homogeneous density) of the fits, indicates that the fit parameters are reasonable for the overall sample. The assumptions and limitations for the fitting procedure and their effect on the fit are described in more detail below (Section 4.4).

The van Genuchten parameter values α and n from the water retention curve fitting were compared to the values based on the commonly used parameterization by Yamaguchi et al. (2012) (Tab. 1). The α values predicted by Yamaguchi et al. (2012) (comparison values in Tab. 1) are between 2 and 4 times smaller than the values obtained by fitting (fitted parameters in Tab. 1). Part of this discrepancy is likely due to hysteresis. Hysteresis is responsible for the offset between the wetting and drying curves of a water retention curve. For snow, the hysteresis factor for α between the wetting and drying curves has been experimentally measured at 1.5 (Adachi et al., 2020) and estimated through modeling to be >2.0 (Leroux et al., 2020). Contrarily, Coléou et al. (1999) found similar heights of the capillary fringe for wetting and drying of pre-wetted snow samples. For soils, a factor of 2 is often used (Kool and Parker, 1987). The ratios obtained here are on the high end of this range and may indicate that other factors increased this apparent hysteresis.

One of these factors is the discrepancy between the methods used to measure the grain size in the parameterization by Yamaguchi et al. (2012) (camera) and in this study (crystal grid card). For example, reducing the grain size of the fine-grained snow from 0.5 mm to 0.25 mm results in an α ratio close to 2. Variations of 0.25 mm in the grain size are well within the measurement error of the visual approach using the crystal grid and the method itself is different from the technique used by Yamaguchi et al. (2012). This discrepancy in grain size measurement methods is a known issue and the results presented here further underline the need for consistency between measurement techniques (Lombardo et al., 2025b). Therefore, it is unclear if the apparent hysteresis in α is really greater for the fine-grained snow compared to the large-grained snow.

For n, the values obtained by the parameterization by Yamaguchi et al. (2012) were 3 and 4 times larger than those obtained by the fitting for $FG_{s,g}$ and FG_s, respectively. For $CG_{s,g}$ and CG_s, the ratios were 0.5 and 1.2, respectively. These discrepancies are more difficult to understand. The relatively large ratios for the fine-grained snow experiments could be a result of the fact that the parametrization by Yamaguchi et al. (2012) was based on measurements with sieved snow, while the snow samples used here were not sieved. Sieving leads to narrower grain size, and thus also pore size, distributions, which are characterized by higher n values (van Lier and Pinheiro, 2018). Hysteresis in n is typically not considered for snow since the experiments by Adachi et al. (2020) showed that it was minimal. However, the experiments by Adachi et al. (2020) consisted of only three measurements using sieved snow with grain sizes greater than 1 mm. Since the fine-grained snow used here was less than 1 mm in diameter, it is possible that there is a grain-size dependence on the hysteresis of snow. However, since we cannot differentiate between possible hysteresis and the effects of sieving, additional studies are needed to determine if hysteresis in n exists for snow.

The n values of the coarse-grained snow experiments are inconsistent due to the high n value of $CG_{s,g}$ (18.6). This value is even higher than that for relatively monodisperse sands (Benson et al., 2014). Therefore, it seems this value is inflated. This was likely caused by a change in density at a height similar to the capillary rise height (Fig. A3), since a reduction in density would lead to a reduction in liquid water content. The true value is therefore likely lower. Since the n value for CG_s is relatively close to the predicted value by Yamaguchi et al. (2012), it seems reasonable to conclude that the coarse-grained snow showed better agreement in n with the literature values than the fine-grained snow.

Differences in the van Genuchten parameter values between this study and literature values can also be related to the spatial variability caused by the asymmetric sample geometry. In contrast to the circular sample cross sections with diameters of 5, 8, and 15 cm in Yamaguchi et al. (2012) and Adachi et al. (2020), we used a rectangular cross-section with one dimension limited by the neutron beam attenuation (1 cm in the beam direction). The filling of this narrow shape is expected to be more heterogeneous compared to the sieving into larger, cylindrical columns used by Yamaguchi et al. (2012) and Adachi et al. (2020). This is manifested in density values that are considerably lower in some regions compared to the averaged dry density (see regions in Fig. 10 with density values below 425 kg m^{-3} compared to averaged dry density of about 530 kg m^{-3}). Such spatial variability is directly related to the expanded width of the pore size distribution as expressed by smaller values of shape parameter n. In addition, the presence of regions with larger porosities, and thus larger pore sizes, aligns with the experimental findings of large α values. This can be seen, for example, in Tab. 1 for $FG_{s,g}$ with an averaged porosity of 0.41, which is

smaller than the saturated water content of 0.46. The capillary forces in larger pores are generally weaker and the α value is correspondingly larger compared to a denser packing.

410 The use of the dry density calculated from the measured optical density (ρ_{OD} in Tab. 1) as opposed to the dry density measured prior to packing ($\rho_{\mu CT}$ in Tab. 1) also had an effect on the water retention curve fitting. Generally speaking, the use of a different density shifts the water retention curve, leading to new fit values. For example, when comparing the fit parameters for $FG_{s,g}$ calculated with ρ_{OD} compared to $\rho_{\mu CT}$, the dry density decreased by 2%, which led to an increase in the saturated liquid water content (θ_s) of 2% (assuming θ_s is equal to the porosity), a decrease in n of 3%, and a decrease in α of 0.5%.

415 Changes in density do not affect the residual liquid water content (θ_r) of these fits since the value was limited to near zero. The results were similar for FG_s, where $\rho_{\mu CT}$ was 6% larger than ρ_{OD}, which led to a decrease in the saturated liquid water content (θ_s) of 8%, an increase in n of 9%, and an increase in α of 2%. Thus, changes in dry density predominantly impact the saturated liquid water content and n parameters. The relatively smaller change in α makes sense since the change in density stretches or shrinks the curve horizontally (with respect to liquid water content), but not vertically (with respect to pressure head).

420 head).

4.3 Fitted values - hydraulic conductivity fitting

~~The~~ Similar to the water retention curve fitting, the MAE can also be used for describing the quality of the inverse fitting of the temporal dynamics. The MAE of the inverse fitting varied from 0.013–0.076 liquid water content, with the MAE generally improving (i.e. becoming smaller) with time. In other words, the fit was generally better towards the end of the experiment, which was due to discrepancies between the simulation and measurements at the beginning of the experiments (discussed in detail in Section 4.4 below). It should be noted that the small MAE values in the first time steps are caused by the thick layer of residual water content; the MAE within the wetted region is considerably larger. The inverse fitting was therefore poorer than the water retention curve fitting. This is further supported by the observation that the experiment (FG_s) with the smallest standard error in the saturated hydraulic conductivity had the largest MAE for the water retention curve. Thus, there is less certainty in the saturated hydraulic conductivity values (K_s) compared to the van Genuchten parameters obtained by the water retention curve fitting. This is likely due to additional fitting of the interfacial layer, which added another free parameter as well as the general increased complexity of the inverse fitting (multiple layers and time dependence) compared to the static water retention curve fitting. These complexities are discussed in more detail below and in Section 4.4.

The saturated hydraulic conductivity values for the snow obtained via the inverse fitting in this study were 20%–60% of the values obtained by the parameterization by Calonne et al. (2012) and are generally consistent with measured the values by Katsushima et al. (2013). A direct comparison with the values by Katsushima et al. (2013) is not possible since SSA was not measured in that study, and the density and grain sizes varied from those used here. In general, however, underestimation of K_s with respect to the parametrization of Calonne et al. (2012) is expected. As described above for the sand, 100% saturation is difficult to achieve experimentally (Yamaguchi et al., 2010) and rapid infiltration of a dry sample traps air within the pores leading to a reduction in saturation. Both of these processes reduce the hydraulic conductivity (Faybishenko, 1995). The

trapping of air during infiltration is not currently accounted for in snowpack models and leads to an overestimation of infiltration rates at short time scales.

The K_s value of the transitional layer below the snow was also a free parameter in the inverse fitting. For the experiments without the gravel layer (FG$_s$ and CG$_s$), the inverse fitting resulted in K_s values for the transitional sand layer of 0.16 cm min^{-1} and 0.15 cm min^{-1}, respectively. These values are 100 times smaller than the reported K_s value of 15.6 cm min^{-1} for this sand (Lehmann et al., 2008). As described above for the flow rates, this is likely due to a combination of factors including dry packing and the braking effect of the gravel-snow and sand-snow interfaces. Additionally, while K_s was the only free parameter in the fitting, it is not the only relevant parameter. Here, the τ parameter, related to the connectivity and tortuosity of the material, was fixed to the default value of 0.5 (Eq. 12). The model was therefore forced to capture changes in τ with K_s. The inclusion of the τ parameter has been suggested as a way to improve estimations of hydraulic conductivity of snow (Yamaguchi et al., 2010). Thus, it is not surprising that the K_s values for the transitional sand layer differ from the reported value.

These effects are also relevant for the experiments with the transitional gravel layer (FG$_{s,g}$ and CG$_{s,g}$), which resulted in K_s values of the transitional gravel layer of 0.3 cm min^{-1} and 3.4 cm min^{-1}, respectively. As with the sand layer, it is to be expected that the dry gravel packing and unsaturated gravel-snow interface led to a relatively small effective hydraulic conductivity. Compared to the sand, the gravel should have a larger saturated hydraulic conductivity as it has larger pores. As such, the fact that these values are larger than those for the transitional sand layer is reasonable. However, it is unclear exactly why the K_s values for the transitional gravel layer differ by an order of magnitude between FG$_{s,g}$ and CG$_{s,g}$. The discrepancy may be due to a poor definition of the hydraulic properties of the transitional layer. The conductivity values at the interface are highly dependent on the liquid configuration within the large interfacial pores. For such a thin region consisting of only a few pores, the formulation of representative hydraulic properties is difficult, considering that the conductivity values are controlled by only these few interfacial pores.

4.4 Limitations of the fitting

Both the fitting of the water retention curve and inverse fitting of the temporal dynamics were fundamentally limited by the uncertainties in determining liquid water content (described in detail below). Thus, the accuracy of the values are proportional to the quality of the liquid water content (more specifically the dry snow density) estimations. The associated errors could be reduced with better execution of the experimental procedure related to inconsistent packing, temperature control, and the delay prior to the first image.

The fitting processes themselves also have some intrinsic limitations. For example, both fitting methods were 1D and used a single set of van Genuchten parameter values for the snowpack and transitional layer below the snow. This means that lateral variations in properties were smoothed and the vertical inhomogeneities (e.g. snow density gradients) within each material were not accounted for. These inhomogeneities are clearly seen in, for example, the strong dip in liquid water content at about 4.5 cm for FG$_s$ (Fig. A5 and Fig. A8) and the optical density images (Fig. 6 and Fig. A2–Fig. A4). Fitting with more materials and/or in 2D is possible and could improve results. However, the number of free parameters increases with the number of

475   unique material layers and thus increases the complexity of the fitting. This is likely only beneficial with improved control of the snowpack properties and packing. A similar argument can be made for allowing the τ parameter to vary.

    For the inverse fitting, there was a discrepancy between the setup of the initial conditions of the model and the physical system. The sand and gravel layers were initialized at the residual water content (θ_r). However, as clearly seen in the initial images (Fig. 7), water had frequently already infiltrated a portion of the sand by the time the first image was taken. Thus,

480   the first image in the experiments was often effectively ahead of the model, since the model was initialized completely dry at t=0. Interestingly, the models quickly overtook the experiments, resulting in higher liquid water contents compared to the experiments even after only 1 timestep. This offset of initial conditions, in combination with the relatively small timesteps used for the fitting at the beginning of the experiment, likely contributed to errors in the inverse fitting . ~~This can be seen in~~ (see discussion of MAE above).

485   There are also some limitations related to the use of MAE as in indicator for fit quality. This is because MAE weights each measurements equally. This has the consequence of treating the bottom of the sample (where most of the changes in liquid water content occur) and the top of the sample (where the samples are mostly dry throughout the experiment) the ~~evolution of the R^2 over time for the nodes used for the fitting (Fig. ??) . The R^2 value increases dramatically during the first several timesteps and then stabilizes. FG_s is an exception in which R^2 achieves its maximum at the beginning of the fit and decreases~~

490   ~~with time. This is due to the relative location of the fitting nodes with respect to the fluctuations in the measurements. For FG_s, the node at 4.25 cm (Fig. A8) coincides with a large reduction in liquid water content and this node shows an increasing reduction in R^2 with each timestep. Thus, the location of the fitting nodes also affects the quality of the fit results and must be considered, particularly when assuming a homogeneous snowpack density.~~ same. Since the simulation is initialized with dry snow, the errors in liquid water content in the lower part of the snow as the water infiltrates are balanced by the many data points

495   with a liquid water content of 0 in the upper part of the snow. This results in a lower MAE than may seem appropriate given the large discrepancy at the bottom of the snow. This effect is more pronounced for the inverse fitting since the water retention curve has a more balanced distribution of wet and dry measurements. This adds additional uncertainty to the interpretation of the hydraulic conductivity fitting. Given the uncertainties of the experiments, analyses of future, more controlled experiments may benefit from an MAE weighted by the liquid water content or a different indicator of the fit quality (e.g. Wasserstein

500   distance).

4.5 Limitations of neutron radiography

As mentioned above, the key limitation of these experiments is the inability to directly distinguish between optical density contributions from water and ice. For the 1D liquid water content profiles, a single value for the dry density was applied to the entire sample (Fig. 8). For the 2D analyses (Fig. 7), a dry density was determined for each pixel. For both methods, the density

505   was assumed to be constant throughout the course of the experiment. Several assumptions and limitations are associated with these approaches.

    For both methods, changes in density over time were not considered. This is potentially problematic due to three processes: melting, settling, and wet-snow metamorphism. Melting was mitigated by cooling the packed columns in an ice bath, using

ice water in the reservoir, and through the use of the climatic chamber. However, no independent measurements of the sample temperature or infiltrating water were possible. Melting is assumed to have caused several artifacts such as some of the liquid water present in the initial images of CG_s and $CG_{s,g}$, as well as the region of high density in Fig. 10. It may also have played a role in the movement seen within the snowpack of $FG_{s,g}$ as shown in the videos provided in the Video Supplement (Lombardo et al., 2025a). Snow is also known to undergo metamorphism in the presence of water (Colbeck, 1986; Brun, 1989). Since the snow samples used in these experiments were melt forms, with the fine-grained snow also containing some small rounded grains, grain-coarsening was likely the predominant metamorphism process. Since grain-coarsening occurs on the timescales of hours (Colbeck, 1986), we do not expect wet-snow metamorphism to dramatically change the snow matrix over the duration of these experiments (maximum of 26 minutes). Settling of the snowpack is not expected to have played a role given the short timescales and minimal snow heights (Marshall et al., 1999).

In addition to possible changes in the snow matrix over time, the initial density distribution was not homogeneous. This is seen in the 2D images (Fig. 7) as well as the 1D optical density profiles (Fig. 8). For the 1D profiles, the use of a single value ignored vertical density gradients, which were particularly prevalent in the coarse-grained snow experiments (CG_s and $CG_{s,g}$). However, this method allowed for the correction of the initial dry density when water was present in the first image. Since the dry density values for the 1D analyses were reasonable compared to the pre-packed values, errors in the 1D profiles are mostly due to the spatial distribution of the snow and likely had the largest effects on the water retention curve fitting.

For the pixel method used for the wetting front analyses, 2D variations in density were accounted for. However, the influence of water in the initial images was not. Thus, uncertainties in the wetting front position are likely for regions with high liquid water contents in the initial images as these dry densities were artificially high.

Ultimately, while neutron radiography provided a high spatio-temporal resolution, the large uncertainties required a reduction in resolution for the fitting. The method therefore provided results on a scale somewhere in between the larger scales typical in the field (>cm, e.g. Techel and Pielmeier (2011)) and the high resolutions of laboratory techniques such as micro-computed tomography and MRI (Adachi et al., 2020; Yamaguchi et al., 2025). Improvements to the experimental procedures, as outlined above, could reduce these uncertainties. Particularly helpful would be obtaining a truly dry image prior to water infiltration. Another option would be to drain the water from the snow after the experiment by lowering the reservoir. The resulting snow structure with residual liquid water could help estimate changes to the snow structure. However, the use of other techniques that can directly differentiate between water and ice, such as time-of-flight radiography with cold neutrons or MRI, will be necessary for providing more detailed measurements (Siegwart et al., 2019; Yamaguchi et al., 2025).

4.6 Implications for future research

Our results have several implications for the future study of capillary-driven processes in snow and their implementation in snowpack models. First, the results suggest that wetting effects such as hysteresis in the water retention and hydraulic conductivity curves, and trapping of air within pores during infiltration should be implemented in snowpack models. Hysteresis has been measured previously and the results here further support the magnitude of the hysteresis (Adachi et al., 2020; Leroux et al., 2020). Additionally, the incomplete saturation of snow is typically assumed to be about 90% of the pore space (Yamaguchi

et al., 2010, 2012), but has been experimentally measured as low as 80% (Adachi et al., 2020). For top-down infiltration, this effect could be even larger as the air is trapped from above. This may have large effects on the dynamics of capillary-driven processes, which are currently not accounted for in most snowpack models.

Second, at the soil-snow interface specifically, the presence of a porous vegetation layer was previously shown to have no effect on the liquid water content within the snow, given that the layers were hydraulically connected and in hydrostatic equilibrium (Lombardo et al., 2025b). Here, under transient conditions, we showed that a relatively dry transitional layer below the snow slowed the flow of water into the snow substantially. Additionally, the timescales for the capillary rise experiments performed here were on the order of minutes, which should be considered when comparing to other relevant snowpack processes such as metamorphism. For glide-snow avalanches specifically, the results demonstrate the importance of considering the the hydraulic properties of the soil-snow interface.

Finally, the results highlight a constant challenge in snow science. Namely, that many discrepancies exist between measurement techniques and their spatio-temporal scales. For example, parameterizations are often determined with high-resolution techniques in the lab, while the parameterizations are then applied to field data with much lower resolution. This was described above for the parameterization by Yamaguchi et al. (2012) and is a good example of how mixing measurement techniques can lead to substantial errors and convolute results. Whereas for dry snow, micro-computed tomography has asserted itself as the gold standard for microstructure measurements, no analogous technique has been proven for wet snow (Lombardo et al., 2025c). Without better measurement techniques, wet snow research will continue to lag behind its dry counterpart. As climate change increases the amount of wet snow in alpine regions, the lack of reliable data on wet snow will become increasingly problematic for snow hydrology and avalanche forecasting models (Mayer et al., 2024).

5 Conclusions

Capillary rise experiments of sand-snow and sand-gravel-snow systems were performed using neutron radiography, providing high resolution (92 μm and 15 s), 2D images of the capillary rise process. The images allowed for quantification of snow water retention curves, flow rates, and hydraulic conductivities. The results showed that both snow grain size and density affected capillary rise height, while the properties of the transitional layer below the snow predominantly influenced the dynamics. When compared to literature, the comparatively large α parameter values obtained in these experiments support the existence of hysteresis in the water retention curve of snow. Additionally, the experiments demonstrated that dry, porous interfaces (here, the gravel) can lead to large reductions in flow rates. The capillary rise process itself was relatively inhomogeneous at the mm to cm scale investigated here, which was shown to depend on the homogeneity of the snow properties. The limited amount of data on snow hydraulic properties and inconsistency between measurement techniques at the laboratory and field scale is problematic for the implementation of the available data in snow models, and will need to be resolved as climate change increases the prevalence and importance of wet snow.

Fine-grained   Coarse-grained

5 mm
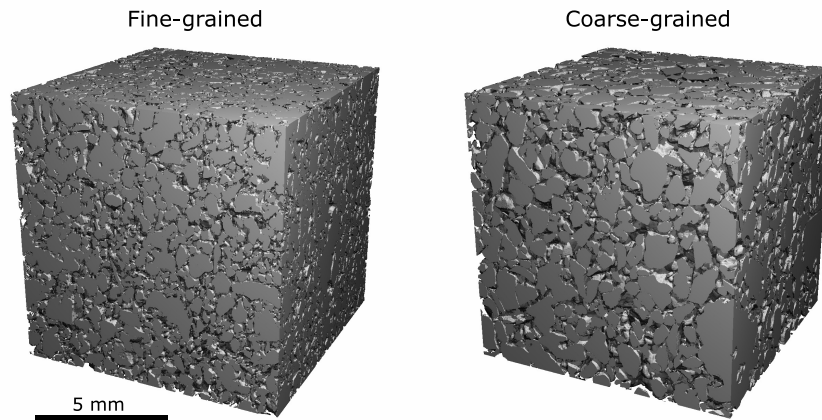
Figure A1. Micro-computed tomography images of the fine-grained (FG) and coarse-grained (CG) snow samples. The snow structure is shown in gray with the pore space in white. The images have a voxel size of 11 μm. Density and specific surface area are provided in Tab. 1.

Data availability. Data for the inverse fitting are available at https://doi.org/10.16904/envidat.572. Other data are available upon request.

575 *Video supplement.* Videos of the experiments are available at https://doi.org/10.16904/envidat.572.

Appendix A: Appendix

A1 Snow microstructure

The snow samples were imaged with μCT to obtain high-resolution measurements of the density and specific surface area (Fig. A1).
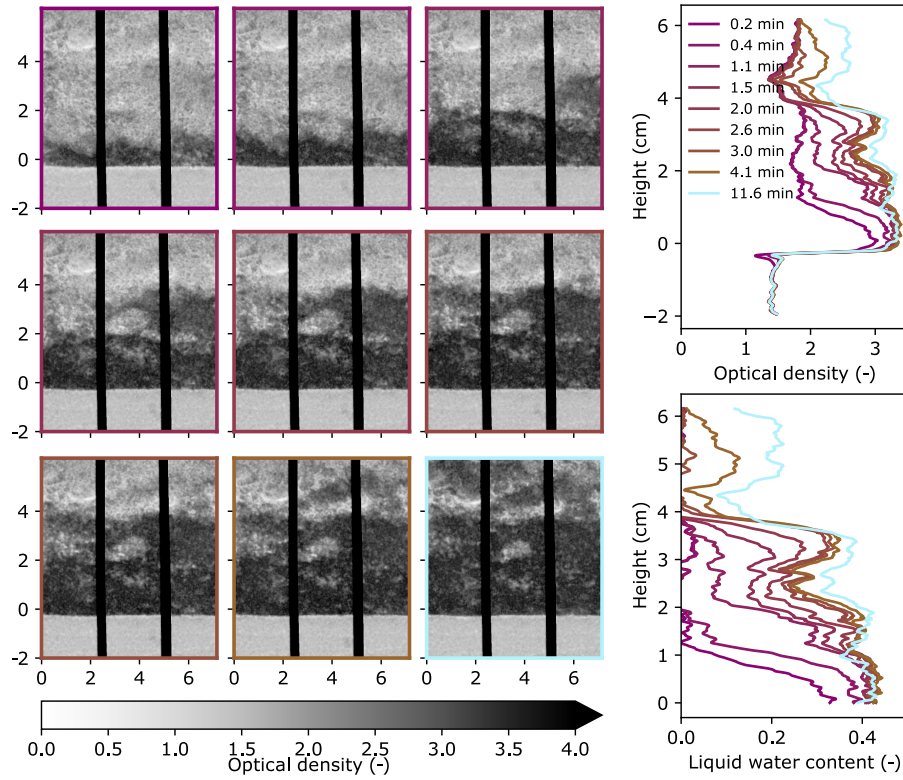
Figure A2. Summary figure of experiment FG$_s$ showing the 2D optical density evolution over time (left), 1D horizontally averaged optical density profile evolution over time (top right), and 1D horizontally averaged liquid water content profile of the snow over time (bottom right). The 2D images correspond to the times in the vertical profiles (right) as indicated by the color. The units for the optical density images (left) are cm for both axes. For the y-axes of all plots in this figure, a height of 0 cm was defined as the height where the continuous snow phase begins, where the effects of the sand-snow transition are no longer present. The vertical black-body bars are shown in black in the images (left).

580 **A2   Summary figures**

The summary figures for FG$_s$, CG$_{s,g}$, and CG$_s$ show the 2D evolution of the optical density and the resulting 1D profiles (Fig. A2-A4).
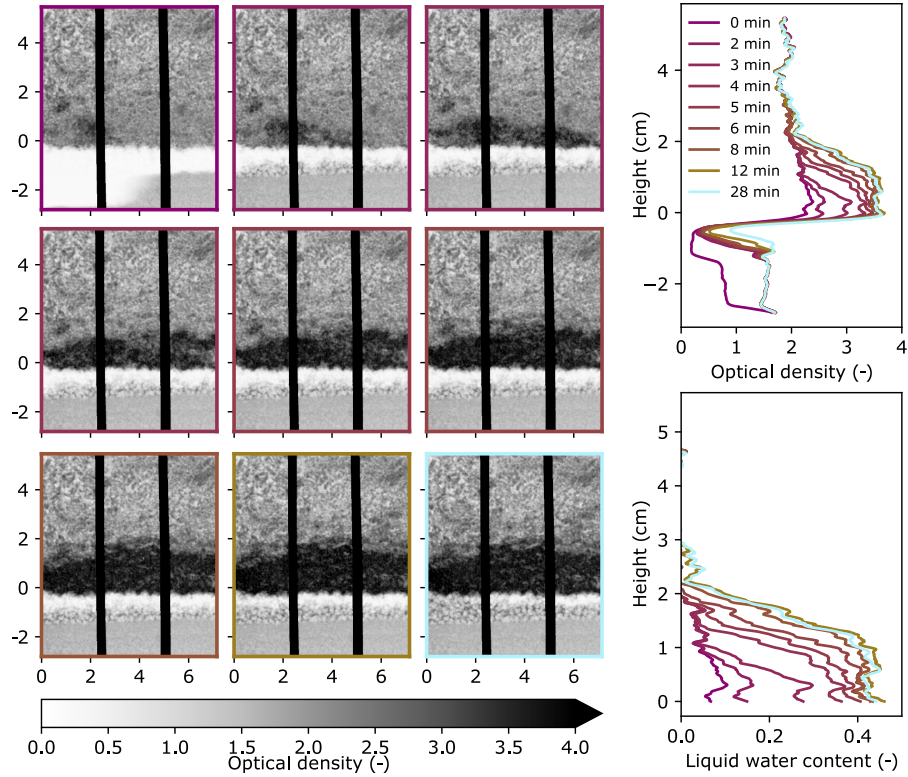
Figure A3. Summary figure of experiment CG$_{s,g}$ showing the 2D optical density evolution over time (left), 1D horizontally averaged optical density profile evolution over time (top right), and 1D horizontally averaged liquid water content profile of the snow over time (bottom right). The 2D images correspond to the times in the vertical profiles (right) as indicated by the color. The units for the optical density images (left) are cm for both axes. For the y-axis of all plots in this figure, a height of 0 cm was defined as the height where the continuous snow phase begins, where the effects of the gravel-snow interface are no longer present. The vertical black-body bars are shown in black in the images (left).
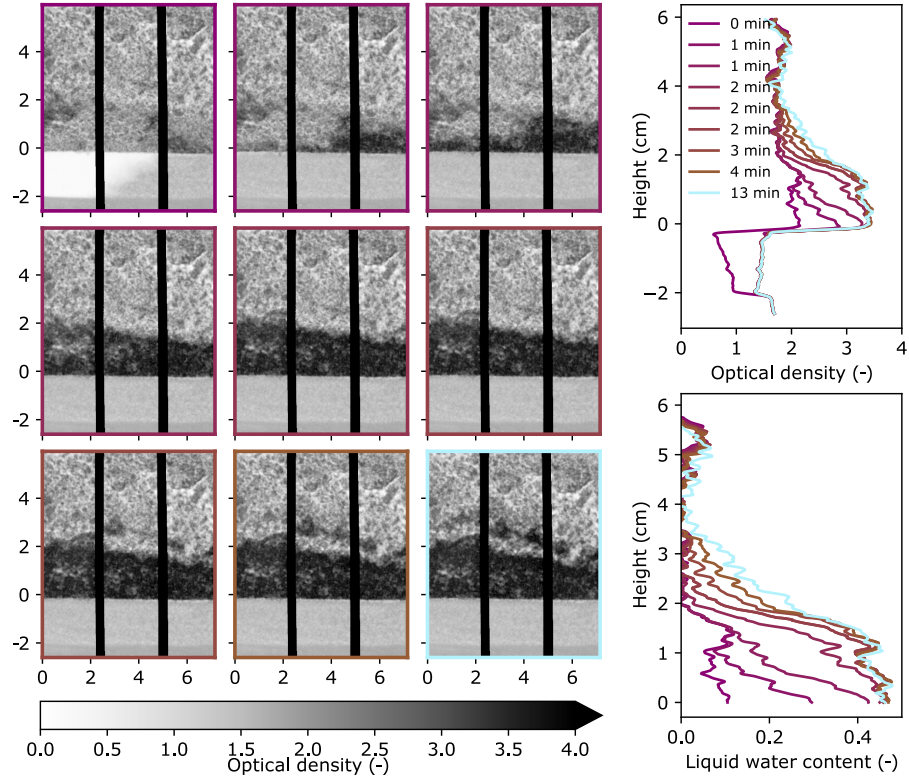
Figure A4. Summary figure of experiment CG_s showing the 2D optical density evolution over time (left), 1D horizontally averaged optical density profile evolution over time (top right), and 1D horizontally averaged liquid water content profile of the snow over time (bottom right). The 2D images correspond to the times in the vertical profiles (right) as indicated by the color. The units for the optical density images (left) are cm for both axes. For the y-axis of all plots in this figure, a height of 0 cm was defined as the height where the continuous snow phase begins, where the effects of the sand-snow transition are no longer present. The vertical black-body bars are shown in black in the images (left).
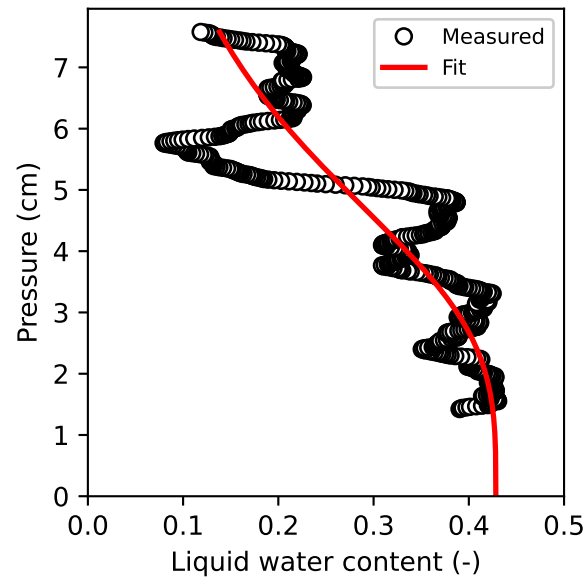
Figure A5. The 1D liquid water content of FG_s as a function of pressure head (black circles) and the fit of these points to Eq. 10 (red line) with ~~R^2=0.75~~ the mean absolute error (MAE) equal to 0.041 and expressed as the volume fraction of liquid water content.

A3   Water retention curve fitting

The water retention curve fitting for FG_s, $CG_{s,g}$, and CG_s show measured liquid water content profiles and resulting fits (Fig. A5-A7).

585
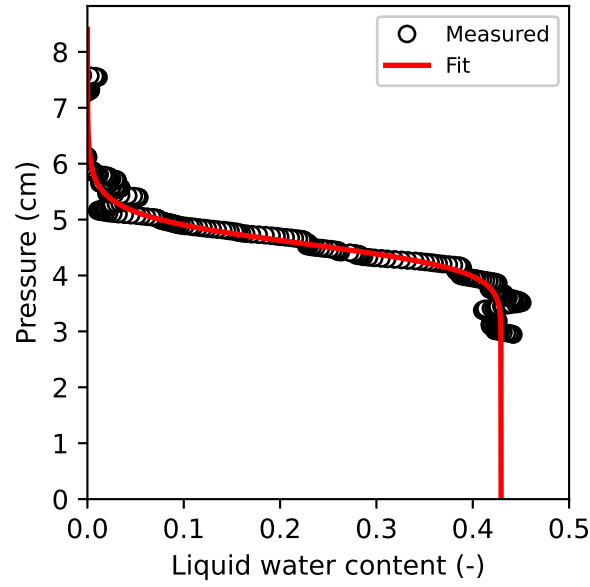
Figure A6. The 1D liquid water content of $CG_{s,g}$ as a function of pressure head (black circles) and the fit of these points to Eq. 10 (red line) with ~~R^2=0.97~~ the mean absolute error (MAE) equal to 0.023 and expressed as the volume fraction of liquid water content.
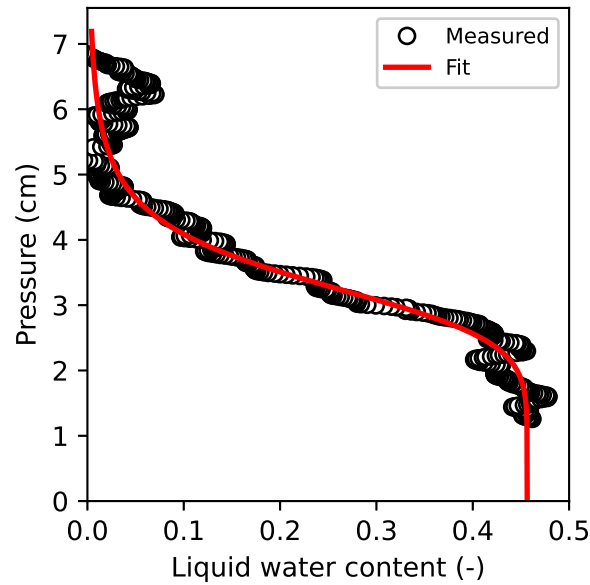
Figure A7. The 1D liquid water content of CG_s as a function of pressure head (black circles) and the fit of these points to Eq. 10 (red line) with ~~R^2=0.98~~ the mean absolute error (MAE) equal to 0.019 and expressed as the volume fraction of liquid water content.
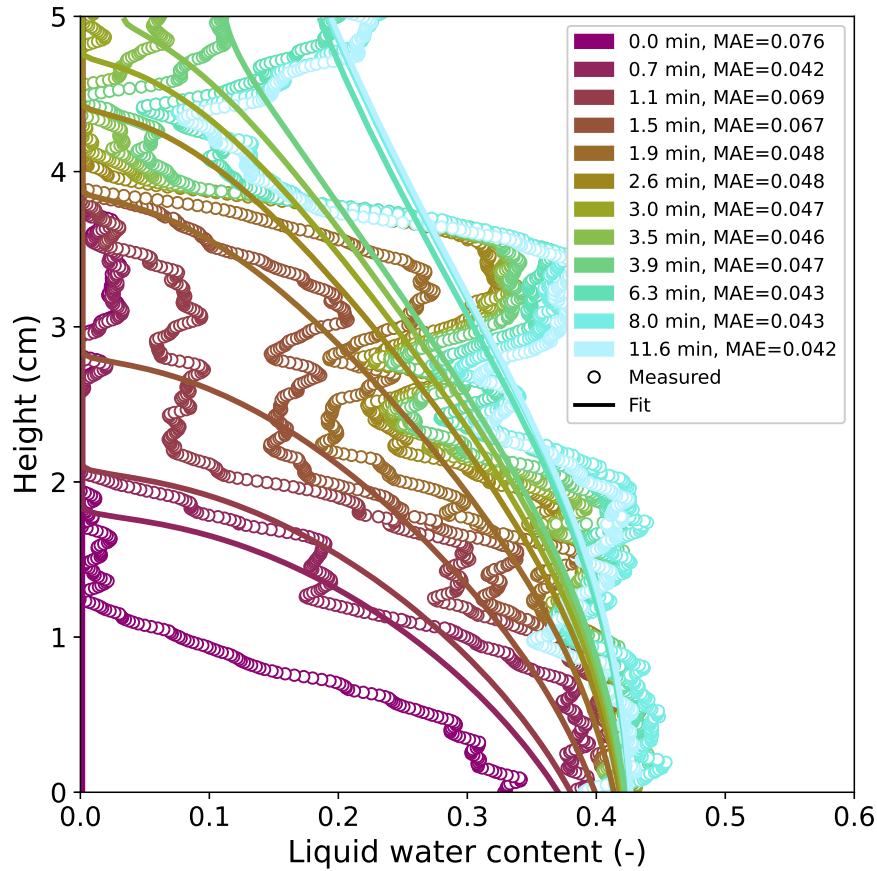
Figure A8. The measured liquid water content profiles and the accompanying inverse fit results for FG$_\text{s}$ with the mean absolute error (MAE) expressed as the volume fraction of liquid water content. Note that the small liquid water content values near 4.5 cm caused a large error in the fitting as shown in Fig. ??.

A4   Hydraulic conductivity fitting

The inverse fitting for FG$_\text{s}$, CG$_\text{s,g}$, and CG$_\text{s}$ show the evolution of the liquid water content profiles and resulting fits (Fig. A8-A10).

The evolution of R^2 for each of the inverse fits at the fitting nodes (i.e. 11 nodes with 0.5 cm spacing). Fitting was performed at each point and the lines are to guide the eye to the evolution of R^2 over time.

590

Author contributions. Conceptualization: All authors; Data curation: ML, AK; Formal analysis: ML, AK, PL; Funding acquisition: JS, PL; Investigation: ML, AK, AF; Methodology: ML, AK, AF, PL; Project administration: All authors; Resources: All authors; Software: ML,
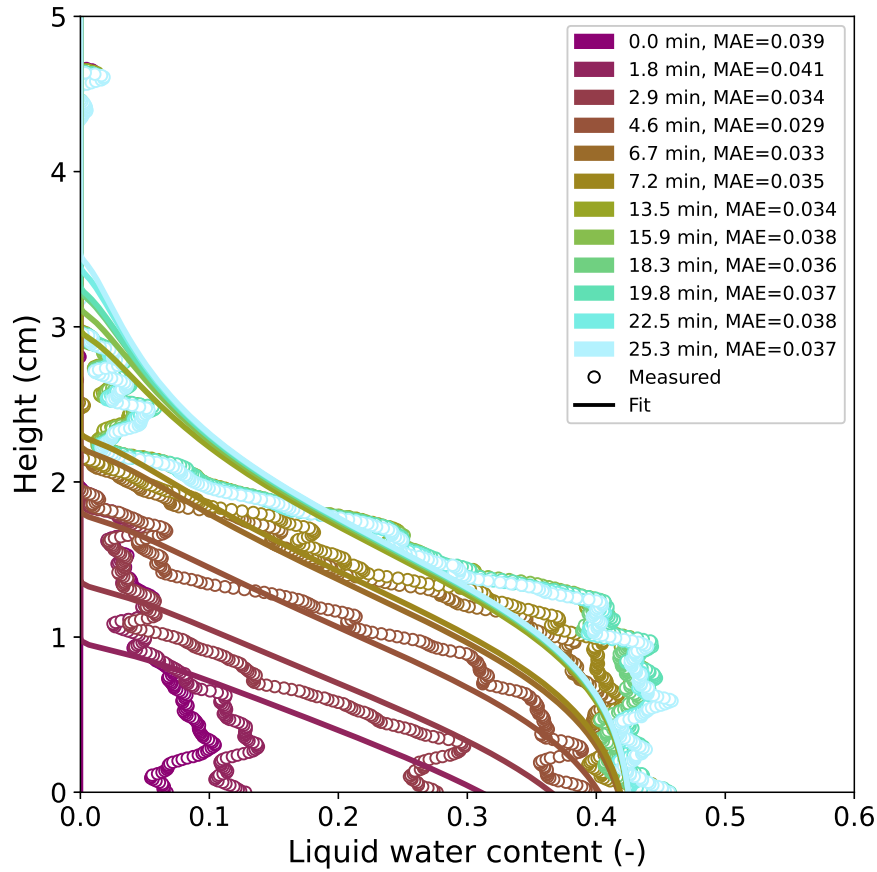
Figure A9. The measured liquid water content profiles and the accompanying inverse fit results for CG$_{s,g}$ with the mean absolute error (MAE) expressed as the volume fraction of liquid water content.

AK; Supervision: AH, JS, PL; Validation: ML, AK, PL; Visualization: ML; Writing - original draft preparation: ML; Writing - review and editing: All authors

595   *Competing interests.* Jürg Schweizer is a member of the editorial board of The Cryosphere.

Acknowledgements. This work is based on experiments performed at the Swiss spallation neutron source SINQ, Paul Scherrer Institute, Villigen, Switzerland. This project was funded by SNSF Grant 200021-212949.
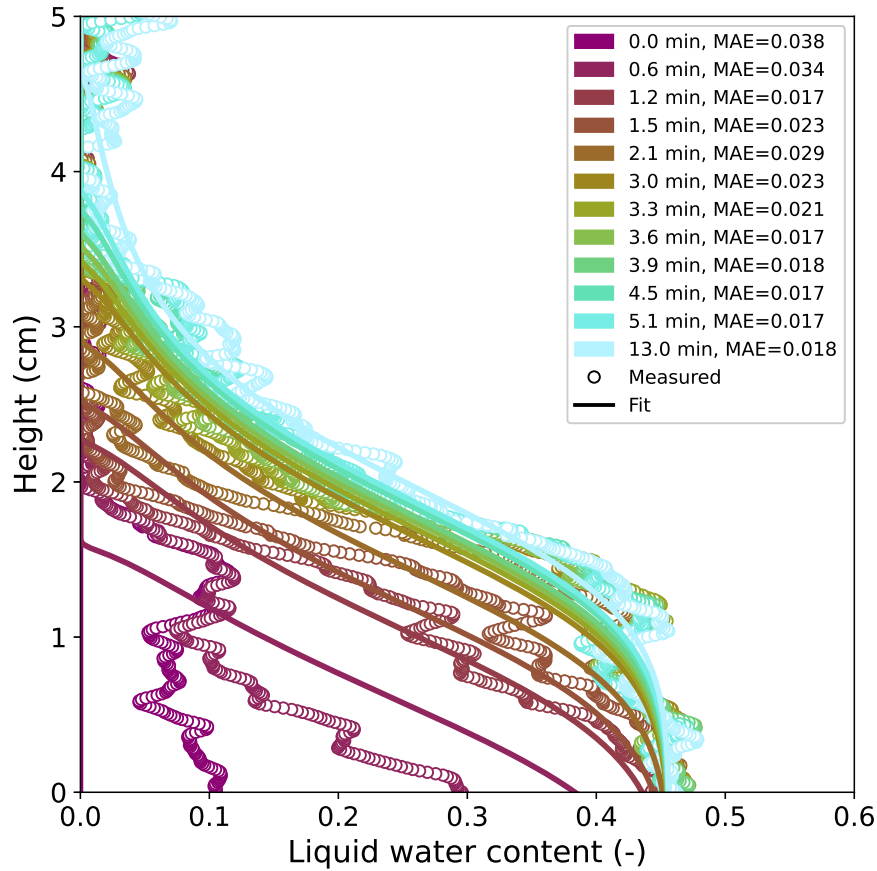
Figure A10. The measured liquid water content profiles and the accompanying inverse fit results for CG$_s$ with the mean absolute error (MAE) expressed as the volume fraction of liquid water content.

References

Adachi, S., Yamaguchi, S., Ozeki, T., and Kose, K.: Application of a magnetic resonance imaging method for nondestructive, three-dimensional, high-resolution measurement of the water content of wet snow samples, Frontiers in Earth Science, 8, https://doi.org/10.3389/feart.2020.00179, 2020.

Albert, M. R., Shultz, E. F., and Perron, F. E.: Snow and firn permeability at Siple Dome, Antarctica, Annals of Glaciology, 31, 353–356, https://doi.org/10.3189/172756400781820273, 2000.

Barella, R., Bavay, M., Carletti, F., Ciapponi, N., Premier, V., and Marin, C.: Unlocking the potential of melting calorimetry: a field protocol for liquid water content measurement in snow, The Cryosphere, 18, 5323–5345, https://doi.org/10.5194/tc-18-5323-2024, 2024.

Benson, C. H., Chiang, I., Chalermyanont, T., and Sawangsuriya, A.: Estimating van Genuchten Parameters α and n for Clean Sands from Particle Size Distribution Data, pp. 410–427, https://doi.org/10.1061/9780784413265.033, 2014.

600

605

Brun, E.: Investigation on Wet-Snow Metamorphism in Respect of Liquid-Water Content, Annals of Glaciology, 13, 22–26, https://doi.org/10.3189/S0260305500007576, 1989.

610 Calonne, N., Geindreau, C., Flin, F., Morin, S., Lesaffre, B., Rolland du Roscoat, S., and Charrier, P.: 3-D image-based numerical computations of snow permeability: links to specific surface area, density, and microstructural anisotropy, The Cryosphere, 6, 939–951, https://doi.org/10.5194/tc-6-939-2012, 2012.

Carminati, C., Boillat, P., Schmid, F., Vontobel, P., Hovind, J., Morgano, M., Raventos, M., Siegwart, M., Mannes, D., Gruenzweig, C., Trtik, P., Lehmann, E., Strobl, M., and Kaestner, A.: Implementation and assessment of the black body bias correction in quantitative neutron

615 imaging, PLoS ONE, 14, 1–24, https://doi.org/10.1371/journal.pone.0210300, 2019.

Clerx, N., Machguth, H., Tedstone, A., Jullien, N., Wever, N., Weingartner, R., and Roessler, O.: In situ measurements of meltwater flow through snow and firn in the accumulation zone of the SW Greenland Ice Sheet, The Cryosphere, 16, 4379–4401, https://doi.org/10.5194/tc-16-4379-2022, 2022.

Colbeck, S.: Grain and bond growth in wet snow, IAHS Publication, 114, 51–61, 1975.

620 Colbeck, S.: Statistics of coarsening in water-saturated snow, Acta Metallurgica, 34, 347–352, https://doi.org/10.1016/0001-6160(86)90070-2, 1986.

Colbeck, S. C.: The capillary effects on water percolation in homogeneous snow, Journal of Glaciology, 13, 85–97, https://doi.org/10.3189/s002214300002339x, 1974.

Coléou, C. and Lesaffre, B.: Irreducible water saturation in snow: experimental results in a cold laboratory, Annals of Glaciology, 26, 64–68,

625 1998.

Coléou, C., Xu, K., Lesaffre, B., and Brzoska, J.-B.: Capillary rise in snow, Hydrological Processes, 13, 1721–1732, https://doi.org/10.1002/(SICI)1099-1085(199909)13:12/13<1721::AID-HYP852>3.0.CO;2-D, 1999.

Courville, Z., Hörhold, M., Hopkins, M., and Albert, M.: Lattice-Boltzmann modeling of the air permeability of polar firn, Journal of Geophysical Research: Earth Surface, 115, https://doi.org/10.1029/2009JF001549, 2010.

630 D'Amboise, C. J. L., Müller, K., Oxarango, L., Morin, S., and Schuler, T. V.: Implementation of a physically based water percolation routine in the Crocus/SURFEX (V7.3) snowpack model, Geoscientific Model Development, 10, 3547–3566, https://doi.org/10.5194/gmd-10-3547-2017, 2017.

Faybishenko, B. A.: Hydraulic Behavior of Quasi-Saturated Soils in the Presence of Entrapped Air: Laboratory Experiments, Water Resources Research, 31, 2421–2435, https://doi.org/10.1029/95WR01654, 1995.

635 Fees, A., van Herwijnen, A., Altenbach, M., Lombardo, M., and Schweizer, J.: Glide-snow avalanche characteristics at different timescales extracted from time-lapse photography, Annals of Glaciology, 65, e3, https://doi.org/10.1017/aog.2023.37, 2025.

Feistl, T., Bebi, P., Dreier, L., Hanewinkel, M., and Bartelt, P.: Quantification of basal friction for technical and silvicultural glide-snow avalanche mitigation measures, Natural Hazards and Earth System Sciences, 14, 2921–2931, https://doi.org/10.5194/nhess-14-2921-2014, 2014.

640 Fierz, C., Armstrong, R., Durand, Y., Etchevers, P., Greene, E., McClung, D., Nishimura, K., Satyawali, P. K., and Sokratov, S.: The International Classification for Seasonal Snow on the Ground, vol. 83 of *HP-VII Technical Documents in Hydrology*, UNESCO-IHP, Paris, France, 2009.

Hagenmuller, P., Chambon, G., Lesaffre, B., Flin, F., and Naaim, M.: Energy-based binary segmentation of snow microtomographic images, Journal of Glaciology, 59, 859–873, https://doi.org/10.3189/2013JoG13J035, 2013.

645 Hammond, J. C. and Kampf, S. K.: Subannual Streamflow Responses to Rainfall and Snowmelt Inputs in Snow-Dominated Watersheds of the Western United States, Water Resources Research, 56, e2019WR026 132, https://doi.org/10.1029/2019WR026132, 2020.

Hendrick, M., Techel, F., Volpi, M., Olevski, T., Pérez-Guillén, C., van Herwijnen, A., and Schweizer, J.: Automated prediction of wet-snow avalanche activity in the Swiss Alps, Journal of Glaciology, 69, 1365–1378, https://doi.org/10.1017/jog.2023.24, 2023.

Hirashima, H., Yamaguchi, S., Sato, A., and Lehning, M.: Numerical modeling of liquid water movement through lay-
650 ered snow based on new measurements of the water retention curve, Cold Regions Science and Technology, 64, 94–103, https://doi.org/10.1016/j.coldregions.2010.09.003, 2010.

Hirashima, H., Avanzi, F., and Wever, N.: Wet-Snow Metamorphism Drives the Transition From Preferential to Matrix Flow in Snow, Geophysical Research Letters, 46, 14 548–14 557, https://doi.org/10.1029/2019GL084152, 2019.

Jordan, P.: Meltwater movement in a deep snowpack 1. Field observations, Water Resources Research, 19, 971–978,
655 https://doi.org/10.1029/WR019i004p00971, 1983.

Jordan, R.: Effects of capillary discontinuities on water flow and water retention in layered snowcovers, Defence Science Journal, 45, 79–91, https://doi.org/10.14429/dsj.45.4107, 1995.

Jordan, R. E., Hardy, J. P., Perron, F. E., and Fisk, D. J.: Air permeability and capillary rise as measures of the pore struc-
ture of snow: An experimental and theoretical study, Hydrological Processes, 13, 1733–1753, https://doi.org/10.1002/(SICI)1099-
660 1085(199909)13:12/13<1733::AID-HYP863>3.0.CO;2-2, 1999.

Katsushima, T., Yamaguchi, S., Kumakura, T., and Sato, A.: Experimental analysis of preferential flow in dry snowpack, Cold Regions Science and Technology, 85, 206–216, https://doi.org/10.1016/j.coldregions.2012.09.012, 2013.

Kool, J. B. and Parker, J. C.: Development and evaluation of closed-form expressions for hysteretic soil hydraulic properties, Water Resources Research, 23, 105–114, https://doi.org/10.1029/WR023i001p00105, 1987.

665 Lehmann, E. H., Vontobel, P., and Wiezel, L.: Properties of the radiography facility NEUTRA at SINQ and its potential for use as European reference facility, Nondestructive Testing and Evaluation, 16, 191–202, https://doi.org/10.1080/10589750108953075, 2001.

Lehmann, P., Assouline, S., and Or, D.: Characteristic lengths affecting evaporative drying of porous media, Phys. Rev. E, 77, 056 309, https://doi.org/10.1103/PhysRevE.77.056309, 2008.

Leroux, N. R., Marsh, C. B., and Pomeroy, J. W.: Simulation of preferential flow in snow with a 2-D non-equilibrium Richards model and
670 evaluation against laboratory data, Water Resources Research, 56, e2020WR027 466, https://doi.org/10.1029/2020WR027466, 2020.

Lombardo, M., Fees, A., Kaestner, A., van Herwijnen, A., Schweizer, J., and Lehmann, P.: Capillary rise experiments in snow using neutron radiography, https://doi.org/10.16904/envidat.572, enviDat [Dataset], 2025a.

Lombardo, M., Fees, A., Udke, A., Meusburger, K., van Herwijnen, A., Schweizer, J., and Lehmann, P.: Capillary suction across the soil-snow interface as a mechanism for the formation of wet basal layers under gliding snowpacks, Journal of Glaciology, p. 1–46,
675 https://doi.org/10.1017/jog.2025.2, 2025b.

Lombardo, M., Lehmann, P., Kaestner, A., Fees, A., van Herwijnen, A., and Schweizer, J.: A method for imaging water transport in soil–snow systems with neutron radiography, Annals of Glaciology, 65, e8, https://doi.org/10.1017/aog.2023.65, 2025c.

Mallett, R., Nandan, V., Stroeve, J., Willatt, R., Saha, M., Yackel, J., Veysière, G., and Wilkinson, J.: Dye tracing of upward brine migration in snow, Annals of Glaciology, p. 1–14, https://doi.org/10.1017/aog.2024.27, 2024.

680 Mannes, D., Schmid, F., Wehmann, T., and Lehmann, E.: Design and Applications of a Climatic Chamber for in-situ Neutron Imaging Experiments, Physics Procedia, 88, 200–207, https://doi.org/10.1016/j.phpro.2017.06.028, 2017.

Marin, C., Bertoldi, G., Premier, V., Callegari, M., Brida, C., Hürkamp, K., Tschiersch, J., Zebisch, M., and Notarnicola, C.: Use of Sentinel-1 radar observations to evaluate snowmelt dynamics in alpine regions, The Cryosphere, 14, 935–956, https://doi.org/10.5194/tc-14-935-2020, 2020.

685 Marsh, P.: Water flux in melting snow covers, pp. 61–124, Elsevier, Amsterdam, The Netherlands, 1991.

Marshall, H., Conway, H., and Rasmussen, L.: Snow densification during rain, Cold Regions Science and Technology, 30, 35–41, https://doi.org/10.1016/S0165-232X(99)00011-7, 1999.

Mayer, S., Hendrick, M., Michel, A., Richter, B., Schweizer, J., Wernli, H., and van Herwijnen, A.: Impact of climate change on snow avalanche activity in the Swiss Alps, The Cryosphere, 18, 5495–5517, https://doi.org/10.5194/tc-18-5495-2024, 2024.

690 Mitterer, C. and Schweizer, J.: Towards a Better Understanding of Glide-Snow Avalanche Formation, in: Proceedings ISSW 2012. International Snow Science Workshop, Anchorage AK, U.S.A., 16-21 September 2012, pp. 610–616, 2012.

Mualem, Y.: A new model for predicting the hydraulic conductivity of unsaturated porous media, Water Resources Research, 12, 513–522, https://doi.org/10.1029/WR012i003p00513, 1976.

Quéno, L., Fierz, C., van Herwijnen, A., Longridge, D., and Wever, N.: Deep ice layer formation in an alpine snowpack: Monitoring and 695 modeling, The Cryosphere, 14, 3449–3464, https://doi.org/10.5194/tc-14-3449-2020, 2020.

Richards, L. A.: Capillary conduction of liquids through porous mediums, Journal of Applied Physics, 1, 318–333, https://doi.org/10.1063/1.1745010, 1931.

Richards, L. A. and Gardner, W.: Tensiometers for Measuring the Capillary Tension of Soil Water, Journal of the American Society of Agronomy, 28, 352–358, https://doi.org/10.2134/agronj1936.00021962002800050002x, 1936.

700 Rösel, A., Farrell, S. L., Nandan, V., Richter-Menge, J., Spreen, G., Divine, D. V., Steer, A., Gallet, J.-C., and Gerland, S.: Implications of surface flooding on airborne estimates of snow depth on sea ice, The Cryosphere, 15, 2819–2833, https://doi.org/10.5194/tc-15-2819-2021, 2021.

Savitzky, A. and Golay, M. J. E.: Smoothing and Differentiation of Data by Simplified Least Squares Procedures., Analytical Chemistry, 36, 1627–1639, https://doi.org/10.1021/ac60214a047, 1964.

705 Schleef, S., Jaggi, M., Löwe, H., and Schneebeli, M.: An improved machine to produce nature-identical snow in the laboratory, Journal of Glaciology, 60, 94–102, https://doi.org/10.3189/2014JoG13J118, 2014.

Shimizu, H.: Air permeability of deposited snow, Contributions from the Institute of Low Temperature Science, A22, 1–32, 1970.

Siegwart, M., Woracek, R., Damián, J. I. M., Tremsin, A. S., Manzi-Orezzoli, V., Strobl, M., Schmidt, T. J., and Boillat, P.: Distinction between super-cooled water and ice with high duty cycle time-of-flight neutron imaging, Review of Scientific Instruments, 90, 1–15, 710 https://doi.org/10.1063/1.5110288, 2019.

Šimůnek, J., van Genuchten, M. T., and Šejna, M.: Development and Applications of the HYDRUS and STANMOD Software Packages and Related Codes, Vadose Zone Journal, 7, 587–600, https://doi.org/10.2136/vzj2007.0077, 2008.

Techel, F. and Pielmeier, C.: Point observations of liquid water content in wet snow - investigating methodical, spatial and temporal aspects, The Cryosphere, 5, 405–418, https://doi.org/10.5194/tc-5-405-2011, 2011.

715 van Genuchten, M.: A Closed-form Equation for Predicting the Hydraulic Conductivity of Unsaturated Soils, Soil Science Society of America Journal, 44, 892–898, https://doi.org/10.2136/sssaj1980.03615995004400050002x, 1980.

van Lier, Q. d. J. and Pinheiro, E. A. R.: An Alert Regarding a Common Misinterpretation of the Van Genuchten α Parameter, Revista Brasileira de Ciência do Solo, 42, e0170 343, https://doi.org/10.1590/18069657rbcs20170343, 2018.

Walter, B., Horender, S., Gromke, C., and Lehning, M.: Measurements of the pore-scale water flow through snow using Fluorescent Particle
720   Tracking Velocimetry, Water Resources Research, 49, 7448–7456, https://doi.org/https://doi.org/10.1002/2013WR013960, 2013.

Wankiewicz, A.: Water pressure in ripe snowpacks, Water Resources Research, 14, 593–600, https://doi.org/10.1029/WR014i004p00593,
1978.

Wankiewicz, A. C.: Water percolation within a deep snowpack field investigations at a site on Mt. Seymour, British Columbia, Ph.D. thesis,
University of British Columbia, https://doi.org/10.14288/1.0053186, 1976.

725 Webb, R. W., Fassnacht, S. R., Gooseff, M. N., and Webb, S. W.: The Presence of Hydraulic Barriers in Layered Snowpacks: TOUGH2
Simulations and Estimated Diversion Lengths, Transport in Porous Media, 123, 457–476, https://doi.org/10.1007/s11242-018-1079-1,
2018.

Webb, R. W., Wigmore, O., Jennings, K., Fend, M., and Molotch, N. P.: Hydrologic connectivity at the hillslope scale through intra-snowpack
flow paths during snowmelt, Hydrological Processes, 34, 1616–1629, https://doi.org/10.1002/hyp.13686, 2020.

730 Wever, N., Fierz, C., Mitterer, C., Hirashima, H., and Lehning, M.: Solving Richards Equation for snow improves snowpack meltwater runoff
estimations in detailed multi-layer snowpack model, The Cryosphere, 8, 257–274, https://doi.org/10.5194/tc-8-257-2014, 2014.

Wever, N., Comola, F., Bavay, M., and Lehning, M.: Simulating the influence of snow surface processes on soil moisture dynamics and
streamflow generation in an alpine catchment, Hydrology and Earth System Sciences, 21, 4053–4071, https://doi.org/10.5194/hess-21-
4053-2017, 2017.

735 Wever, N., Vera Valero, C., and Techel, F.: Coupled Snow Cover and Avalanche Dynamics Simulations to Evaluate Wet Snow Avalanche
Activity, Journal of Geophysical Research: Earth Surface, 123, 1772–1796, https://doi.org/10.1029/2017JF004515, 2018.

Wever, N., Rossmann, L., Maaß, N., Leonard, K. C., Kaleschke, L., Nicolaus, M., and Lehning, M.: Version 1 of a sea ice module for the
physics-based, detailed, multi-layer SNOWPACK model, Geoscientific Model Development, 13, 99–119, https://doi.org/10.5194/gmd-
13-99-2020, 2020.

740 Würzer, S., Wever, N., Juras, R., Lehning, M., and Jonas, T.: Modelling liquid water transport in snow under rain-on-snow conditions -
Considering preferential flow, Hydrology and Earth System Sciences, 21, 1741–1756, https://doi.org/10.5194/hess-21-1741-2017, 2017.

Yamaguchi, S., Katsushima, T., Sato, A., and Kumakura, T.: Water retention curve of snow with different grain sizes, Cold Regions Science
and Technology, 64, 87–93, https://doi.org/10.1016/j.coldregions.2010.05.008, 2010.

Yamaguchi, S., Watanabe, K., Katsushima, T., Sato, A., and Kumakura, T.: Dependence of the water retention curve of snow on snow
745   characteristics, Annals of Glaciology, 53, 6–12, https://doi.org/10.3189/2012AoG61A001, 2012.

Yamaguchi, S., Adachi, S., and Sunako, S.: A novel method to visualize liquid distribution in snow: superimposition of MRI and X-ray CT
images, Annals of Glaciology, 65, e11, https://doi.org/10.1017/aog.2023.77, 2025.